



NUMERICAL INVESTIGATION OF CAVITY-VANE INTERACTIONS
WITHIN THE
ULTRA COMPACT COMBUSTOR

THESIS

Jonathan Anisko, 2d Lt, USAF

AFIT/GAE/ENY/06-M01

DEPARTMENT OF THE AIR FORCE
AIR UNIVERSITY

AIR FORCE INSTITUTE OF TECHNOLOGY

Wright-Patterson Air Force Base, Ohio

APPROVED FOR PUBLIC RELEASE; DISTRIBUTION UNLIMITED.

The views expressed in this thesis are those of the author and do not reflect the official policy or position of the United States Air Force, Department of Defense, or the United States Government

AFIT/GAE/ENY/06-M01

NUMERICAL INVESTIGATION OF CAVITY-VANE INTERACTIONS
WITHIN THE
ULTRA COMPACT COMBUSTOR

THESIS

Presented to the Faculty
Department of Aeronautics and Astronautics
Graduate School of Engineering and Management
Air Force Institute of Technology
Air University
Air Education and Training Command
In Partial Fulfillment of the Requirements for the
Degree of Master of Science in Aeronautical Engineering

Jonathan Anisko, B.S.

2d Lt, USAF

March 2006

APPROVED FOR PUBLIC RELEASE; DISTRIBUTION UNLIMITED.

NUMERICAL INVESTIGATION OF CAVITY-VANE INTERACTIONS
WITHIN THE
ULTRA COMPACT COMBUSTOR

Jonathan Anisko, B.S.
2d Lt, USAF

Approved:

/signed/

23 Mar 2006

Dr. Ralph Anthenien (Chairman)

date

/signed/

23 Mar 2006

Dr. Mark Reeder (Member)

date

/signed/

23 Mar 2006

Dr. Paul King (Member)

date

Abstract

A numerical analysis and design optimization of the Ultra Compact Combustor (UCC) has been conducted. The UCC is a combustor designed to incorporate high-g loadings to increase flame propagation speed while reducing flame length, thereby helping to significantly reduce the size of a combustor. A commercial CFD package with a $k-\epsilon$ turbulence model has been used to develop design rules for the construction of future UCCs. There have been several versions of UCC that have been designed, built and tested by AFRL/PRTC. Since real experimental tests are expensive and construction time is prohibitive to test many different design configurations, CFD modeling of the UCC is used to speed up the design optimization process while reducing the overall costs.

The CFD models have been validated by comparison to data from recent experimental tests. The use of periodic sections and grid independence were validated as well. Modifications to the physical configuration were then modeled using CFD. Shortening the cavity to 38.1 mm and then to 25.4 mm was investigated. On the shortest cavity configuration the air inlets were canted to higher angles, from initially 37° to 45° and then 55° . Next, the radial vane was aerodynamically improved with a rounded aft corner in addition to air inlets introduced into the leading edge of the vane. The final configuration included increasing the vane height from the baseline dimensions. The modified combustors were all compared using exhaust samples, combustion efficiency, pattern and profile factors, as well as flow visualization.

The shortening of the cavity was found to reduce the harmful emissions in the exhaust. Increasing the angle of the air inlets further improved the emissions by increasing the residence time of the fuel particles in the cavity. Aerodynamically improving the vane reduced the pressure loss of the combustor by up to 25%. The increased vane height was an initial step in scaling up the UCC to operational configurations. Of the models in this research, the most improved configuration was found to be the 45° air inlet on the shortest cavity.

Acknowledgements

I would like to express my sincere appreciation to my advisor, Dr. Ralph Anthenien, for his guidance, explanations, patience, support, and all the time spent editing and revising my writings. I thank the Watson Scholars Initiative for giving myself and my fellow Scholars the opportunity to attend AFIT and earn our Masters degrees.

I would also like to thank Dr. Julian Tishkoff from the Air Force Office of Scientific Research/NA and Dr. Robert Hancock from Air Force Research Laboratory/PRTC for their financial support in this research. My appreciation also goes to Dr. Joe Zelina and Capt. Roger Greenwood for their support and assistance in this thesis.

I also appreciate the support that all my fellow Scholars and students gave me throughout the entire time we shared at AFIT.

Finally, I would like to thank my family for their support throughout this experience. I especially thank my wife for her constant encouragement and love throughout this entire endeavor.

Jonathan Anisko

Table of Contents

	Page
Abstract	iv
Acknowledgements	v
List of Figures	ix
List of Tables	xii
List of Symbols	xiv
List of Abbreviations	xvi
I. Introduction and Overview	1
1.1 Motivation	1
1.2 Ultra Compact Combustor	2
1.3 Benefits	3
1.4 Combustor Design Parameters	4
1.5 Thesis Outline	5
II. Background and Theory	6
2.1 Literature Review	6
2.1.1 Conventional Combustor Layout	6
2.1.2 Trapped Vortex Combustion	7
2.1.3 Centrifugal Force Combustion	8
2.1.4 Inter Turbine Burner	9
2.1.5 UCC	10
2.2 Computational Fluid Dynamics	13
2.2.1 CFD History	13
2.2.2 Turbulence Modeling	13
2.2.3 Wall Functions	14
2.2.4 Species Modeling	16
2.2.5 Emissions	17
2.2.6 NO_x Modeling	18
2.2.7 Post Processing	19
2.3 Heat Transfer	19
2.4 Pattern and Profile Factors	20

	Page
III. Methodology	22
3.1 Experimental Results for Validation	22
3.2 Numerical Methods	24
3.2.1 Grid Development	25
3.2.2 Discrete Phase Model	26
3.2.3 Fuel Injections	26
3.2.4 Species Modeling	26
3.2.5 Pollutant Process Modeling	28
3.2.6 Boundary Conditions	28
3.2.7 Convergence Criteria	29
3.3 Comparison Criteria	30
3.3.1 Combustion Efficiency	30
3.3.2 Pressure Drop	31
3.3.3 G-Loading	31
3.3.4 Periodic Boundaries	32
IV. Results and Discussion	33
4.1 Validation of the CFD Model	33
4.1.1 Comparison	33
4.1.2 Pattern and Profile	35
4.2 Base Model	38
4.2.1 Species and Efficiency	39
4.2.2 Internal Flow Investigation	39
4.2.3 Pattern and Profile	40
4.3 Shortened Cavity Model	43
4.3.1 Species and Efficiency	43
4.3.2 Internal Flow Investigation	44
4.3.3 Pattern and Profiles	45
4.4 Increased Air Injection Angle Models	47
4.4.1 Species and Efficiency	47
4.4.2 Internal Flow Investigation	49
4.4.3 Pattern And Profile	50
4.4.4 Fuel Particle Tracks	51
4.5 Aerodynamically improved Vane	54
4.5.1 Species and Efficiency	54
4.5.2 Internal Flow Investigation	55
4.5.3 Pattern and Profile	56
4.6 Tall Vane Model	57
4.6.1 Species and Efficiency	59
4.6.2 Internal Flow Investigation	60

	Page
4.6.3 Pattern and Profile	61
4.7 Circumferential Velocity Calculations	63
4.8 Emissions Comparisons	65
4.9 Profile Comparisons	66
V. Conclusions	68
5.1 Research Overview	68
5.2 Results Synopsis	68
5.3 Future Work	70
Appendix A. Additional Numerical Data	72
A.1 Extra Tables	72
Appendix B. Emissions and Profile	75
Bibliography	79
Vita	81

List of Figures

Figure		Page
1.	Typical gas turbine combustor configuration adapted from Lefebvre [13]	6
2.	Trapped Vortex Combustion Concept Schematic [22]	8
3.	T-s Diagram for Conventional Combustor and ITB modified from Liu and Sirignano (Used without Permission) [17]	10
4.	UCC Experimental Configuration Schematic [21]	11
5.	Integration of the UCC and Turning Vanes (Used with Permission from Anthenien et al. [2]	11
6.	Two views of the UCC configuration	23
7.	Periodic Section of the UCC	24
8.	Temperature Contours on the Coarse Model with LMLP Loading Condition at the Exit Plane	36
9.	Average Circumferential Temperatures at the Exit Plane for the Coarse, Dense and Full UCC Models on LMLP	37
10.	Velocity Vectors colored by Static Temperature on the Radial Plane Midline Plane for Baseline Model on LMLP Loading Conditions	40
11.	Velocity Vectors Colored by Temperature on Same Axial Plane with Front Air Inlet of Baseline Model for LMLP Loading Condition	40
12.	Average Circumferential Temperatures at the Exit Plane for the Baseline Model on the Five Loading Conditions	42
13.	Temperature Contours on the Baseline Model with LMLP Loading Condition at the Exit Plane	42
14.	Velocity Contours Colored by Temperature on Same Axial Plane with Front Air Inlet of Inch37 Model for LMLP Loading Condition	45
15.	Velocity Vectors Colored by Temperature on same axial Location as the Front Air inlets of the Inch Cavity Model	45

Figure		Page
16.	Temperature Contours on the Inch37 Model with LMLP Loading Condition at the Exit Plane	46
17.	Average Circumferential Temperatures at the Exit Plane for the Inch37 Model on the Five Loading Conditions	47
18.	Velocity Vectors Colored by Temperature on Same Axial Plane with Front Air Inlet of Inch45 and Inch55 Model for LMLP Loading Condition	49
19.	Front Air Inlet Velocity Contours Colored by Temperature for Shorter Cavity Models	50
20.	Average Circumferential Temperatures at the Exit Plane for the Inch45 and Inch55 Model on the Five Loading Conditions. The Dotted Lines represent the 55° Model and the Solid Lines Represent the 45° Model	52
21.	Temperature Contours on the Inch45 and Inch55 Models with LMLP Loading Condition at the Exit Plane	52
22.	Fuel Particle Tracks on One Inch Cavity model with 37° air inlets. Lines are Colored by Residence Time	53
23.	Fuel Particle Tracks on Shorter Cavity Model with Increased air Inlets Angles. Lines are Colored by Residence Time	53
24.	Velocity Vectors Colored by Temperature on Same Axial Plane with Front Air Inlet of Nozzle Model for LMLP Loading Condition	56
25.	Velocity Vectors Colored by Temperature on Same Axial Plane with Front Air Inlet of Nozzle Model for LMLP Loading Condition	56
26.	Average Circumferential Temperatures at the Exit Plane for the Nozzle Model on the Five Loading Conditions	58
27.	Tall Vane Plane in line with the Front Cavity Air Inlets	61
28.	Velocity Vectors Colored by Temperature on Same Axial Plane with Front Air Inlet of TallVane Model for LMLP Loading Condition	61
29.	Average Circumferential Temperatures at the Exit Plane for the TallVane Model on the Five Loading Conditions	63

Figure		Page
30.	Temperature Contours on the TallVane Model with LMLP Loading Condition at the Exit Plane	63
31.	Circumferential Velocity vs CLP	64
32.	NO_x on the Exit Plane vs g-loading	65
33.	Carbon Monoxide on the Exit Plane vs g-loading	66
34.	Average Circumferential Temperatures at the Exit Plane for the Seven Models on the LMLP Loading Condition	67
B.1.	Unburned Hydrocarbons on the Exit Plane vs g-loading	75
B.2.	Combustion Efficiency on the Exit Plane vs g-loading	75
B.3.	Average Circumferential Temperatures at the Exit Plane for the Coarse Model on the Five Loading Conditions.	76
B.4.	Average Circumferential Temperatures at the Exit Plane for the Seven Models on the LMLP Loading Condition	76
B.5.	Average Circumferential Temperatures at the Exit Plane for the Seven Models on the LMMP Loading Condition	77
B.6.	Average Circumferential Temperatures at the Exit Plane for the Seven Models on the HMHP Loading Condition	77
B.7.	Average Circumferential Temperatures at the Exit Plane for the Seven Models on the MMHP Loading Condition	78
B.8.	Average Circumferential Temperatures at the Exit Plane for the Seven Models on the LMHP Loading Condition	78

List of Tables

Table		Page
1.	Experimental Loading Conditions	22
2.	Numerical Models	25
3.	Fuel Injection Model	27
4.	Validation Data for Coarse, Dense and Experimental	34
5.	Species and Efficiency Data for the Baseline Model Compared to the Coarse Model Data	38
6.	Pattern and Profile Data for Baseline compared to the Coarse Model Data	41
7.	Species and Efficiency Data for the Inch37 Model Compared to the Baseline Model Data	43
8.	Pattern and Profile Data for Inch37 compared to the Baseline Model Data	46
9.	Species and Efficiency Data for the Inch37 Model Compared to the Inch45 and Inch55 Model Data	48
10.	Pattern and Profile Data for Inch37 compared to the Inch45 and Inch55 Model Data	51
11.	Species and Efficiency Data for the Nozzle Model Compared to the Baseline Model Data	55
12.	Pattern and Profile Data for Nozzle Model compared to the Baseline Model Data	57
13.	Species and Efficiency Data for the TallVane Model Compared to the Baseline Model Data	60
14.	Pattern and Profile Data for TallVane Model compared to the Baseline Model Data	62
A.1.	Species and Efficiency Data for the Coarse Model Compared to the Experimental Data	72
A.2.	Case 1 (LMPL) Loading Condition for the Different Model Configurations	72

Table		Page
A.3.	Case 2 (LMMP) Loading Condition for the Different Model Configurations	73
A.4.	Case 3 (HMHP) Loading Condition for the Different Model Configurations	73
A.5.	Case 4 (MMHP) Loading Condition for the Different Model Configurations	73
A.6.	Case 5 (LMHP) Loading Condition for the Different Model Configurations	74
A.7.	DPM Wall Interaction Comparison on Baseline Model with LMLP Loading Conditions	74

List of Symbols

Symbol		Page
g	Acceleration of Gravity ($\frac{m}{s^2}$)	3
NO_x	Oxides of Nitrogen	4
CO	Carbon Monoxide	4
O_2	Oxygen	4
CO_2	Carbon Dioxide	4
ϕ	Equivalence Ratio	6
S_B	Flame Propagation Speed ($\frac{m}{s}$)	8
μ_t	Turbulent Viscosity ($\frac{kg}{m \cdot s}$)	13
k	Turbulent Kinetic Energy ($\frac{m^2}{s^2}$)	14
ϵ	Turbulent Dissipation Rate ($\frac{m^2}{s^3}$)	14
y^+	Turbulent Wall Unit	15
f	Mixture Fraction	17
H_2O	Water	17
N_2	Nitrogen	17
\bar{N}_{uD}	Nusselt Number	19
\bar{h}	Convective Heat Transfer Coefficient ($\frac{W}{m^2 K}$)	19
Pr	Prandtl Number	20
ν	Kinematic Viscosity($\frac{m^2}{s}$)	20
T_∞	Far Field Temperature (K)	20
T_s	Surface Temperature (K)	20
Ra	Rayleigh Number	20
T_{4max}	Maximum Outlet Temperature (K)	21
T_3	Mean Inlet Temperature (K)	21
T_4	Mean Exit Temperature (K)	21
T_{mr}	Maximum Circumferential Mean Temperature (K)	21

Symbol		Page
\dot{m}_{cav}	Cavity Mass Flow Rate ($\frac{kg}{s}$)	22
V	Cavity Volume (m^3)	22
P_{T_3}	Total Inlet Pressure (Pa)	22
P_{OP}	Operating Pressure (Pa)	27
H_C	Heat of Combustion ($\frac{kJ}{kg}$)	30
EI	Emissions Index ($\frac{g_{pollutant}}{kg_{fuel}}$)	30
U_θ	Circumferential Velocity ($\frac{m}{s}$)	31

List of Abbreviations

Abbreviation		Page
UCC	Ultra Compact Combustor	1
CFD	Computational Fluid Dynamics	1
TVC	Trapped Vortex Combustion	2
ITB	Inter Turbine Burner	3
MTBM	Mean Time Between Maintenance	3
RQL	Rich Quench Lean Burn	4
UHC	Unburned Hydrocarbons	6
AFRL	Air Force Research Laboratory	7
LBO	Lean Burn Out	8
PDF	Probability Density Function	17
CLP	Combustion Loading Parameter	22
LMLP	Low Mass Low Pressure	22
LMMP	Low Mass Medium Pressure	22
HMHP	High Mass High Pressure	22
MMHP	Medium Mass High Pressure	22
LMHP	Low Mass High Pressure	22
IGES	Initial Graphics Exchange Specification	25
DPM	Discrete Phase Model	26

NUMERICAL INVESTIGATION OF CAVITY-VANE INTERACTIONS WITHIN THE ULTRA COMPACT COMBUSTOR

I. Introduction and Overview

1.1 Motivation

Decreasing the weight of aircraft components is a major driving force in aerospace design. Designing lighter and more powerful aero-engines has been a major influence in gas turbine technology throughout its short history. One of recent focus in this endeavor is the combustor. A limiting factor in combustor design is that a fuel droplet takes a certain amount of time to completely evaporate and react. In a conventional, axially oriented combustor the length of the combustor is determined by the flow speed of the combustor and the burn time of the fuel. Improvements in flame speed need to be made in order to shrink the combustor. The Ultra Compact Combustor (UCC) uses circumferential burning and high g-loading to significantly shorten the necessary length and weight of a gas-turbine combustor.

Designing a combustor has changed considerably in recent years. With the improvements in computer processing speed and numerical methods for modeling fluid flow, Computational Fluid Dynamics (CFD) is now a fundamental step in the design process. It is significantly cheaper and faster to construct a numerical mesh and test it than to cut metal and test it experimentally. CFD can now be a preliminary method to test various configurations and concepts without the high initial costs of constructing an experimental configuration. However, CFD is still somewhat limited in what it can model. Therefore accuracy needs to be validated to experimental or known data and then CFD can serve as a tool that can compliment experimental research.

1.2 Ultra Compact Combustor

To improve the performance of a combustor, designers have to moderate the temperatures inside the engine as to not surpass the material limits of the engine components. This while maximizing the use of the volume of the combustor to help decrease the overall weight of the engine. The combustor makes up a significant portion of the size of the engine and decreasing the size of this will help with the weight reduction that is at the heart of aeronautical design. Swirl has been introduced into many combustors to help control stability and improve mixing over bluff body methods [13].

The UCC offers a different approach to the typical swirl-stabilized combustor. Air is injected into a cavity running around the outside circumference of the combustor. The air is injected in a circumferential direction to impart high tangential velocities that result in high centrifugal forces around the main body of the combustor. This feature aids in increasing the mixing and flame stretch and therefore the flame speed as well. Further, the high g-loading causes a density stratification, trapping the higher density unreacted (cold) fuel and air in the cavity. The hot, reacted products are buoyantly driven towards the center of the engine and out of the cavity into the main flow.

The UCC is loosely based on the Trapped Vortex Combustion (TVC) concept. It was found that if a cavity is created with proper depth and length conditions a stable locked vortex would be created in that cavity [16]. A significant advantage to the trapped vortex is that the initial burning is out of the high speed main flow. The TVC concept also provides a cavity where the cavity flow may have velocity directed perpendicular to the main flow. This is the principle of the UCC; high g-loading due to centripetal acceleration results. Lewis [14] previously showed the benefit of having combustion occur in high g-loading. A typical laminar flame travels at about 0.5 m/s in a hydrocarbon-air mixture. Turbulent flame speeds can be from 1 - 10 m/sec, due to increased mixing of turbulent flows.

Lewis [14] examined high-g loading of a hydrocarbon-air mixture and found that from 500 g-3500 g the flame propagation speed is proportional to the square root of the g-loading, resulting in flame speeds from around 35 to 100 m/s. The UCC operates in the region of 800-4500 g which leads to greatly reduced reaction times and mixing times due to the increased flame propagation rates.

The reduced reaction time leads to a decreased minimum combustor length. If the combustor length can be sufficiently reduced, a practical aero-gas turbine Inter Turbine Burner (ITB) cycle may result. The ITB cycle introduces a burner between the high and low-pressure turbine stages to act as a second heat addition. This can increase the specific thrust by over 50% without the high thrust specific fuel consumption associated with afterburners [23]. The goal of the UCC is to become short enough to enable an aero-ITB cycle. If the stator is included in the combustor and use of the high swirl flow off the compressors is employed to drive the high g swirl, the potential length savings of the combustor is 66% off conventional designs [2].

1.3 Benefits

The potential benefits in utilizing a UCC include minimizing weight, decreasing harmful emissions, dropping pressure and improving temperature control. Other secondary benefits may occur from the combination of the use of the UCC and the ITB. The addition of the reheat cycle between the high and low pressure turbines can provide power for an ultra high bypass ratio fan or generators to power unmanned aerial vehicles avionics and equipment [26]. With the smaller combustor the UCC will need to react the fuel in a smaller volume than standard combustor configurations. The UCC uses the high-g forces to increase the mixing and flame speeds which aid in using the volume more efficiently. For the same thrust with two combustion stages, less fuel needs to be added for each stage, keeping temperatures down and leading to an increased mean time between maintenance (MTBM) [8].

Combustors must now be constructed with the effort to try to minimize harmful emissions and comply with ever more stringent government regulations on the envi-

ronment. While high combustion temperatures are a result of high specific thrust and high cycle efficiency, they also produce large amounts of oxides of nitrogen (NO_x). The UCC is predicted to behave as an Rich Quench Lean Burn (RQL) combustor which will produce benefits in reducing the amount of NO_x and carbon monoxide (CO). The RQL behavior of the UCC results from an initial reaction that occurs in the combustor's cavity at higher equivalence ratios [24]. The UCC is designed to take advantage of this. This rich burn helps keep the temperatures in the cavity lower which decreases the amount of NO_x produced [13]. As the rich cavity products enter the main airflow the combustion products burn lean. The lean reaction that results will help react the CO , a product from the rich cavity, with the excess oxygen O_2 in the main channel [24]. These combine to form carbon dioxide CO_2 .

1.4 Combustor Design Parameters

Lefebvre [13] has outlined 11 basic requirements that should be obeyed in the designing of a functional combustor. Not all the requirements will be looked at in this design process but some of the key aspects will be examined extensively to evaluate the combustor's performance of the various geometric configurations and loading conditions. The parameters of interest will include combustion efficiency, temperature pattern at the exit plane of the combustor, emissions and pressure loss.

In addition to the above criteria two more will be looked at that are particularly of interest for the UCC. The circumferential velocity in the cavity will be evaluated to aid in determining the g-loading in the combustor's cavity. The main focus of the research is to improve the mass extraction of the cavity combustion gases down radially into the main flow. The amount of the high temperature combustion gases brought down into this main flow can be quantified by the profile and pattern factors of the combustor's exit plane. These quantities are effective in quantifying the spread of the highest temperature gases at the location.

1.5 Thesis Outline

The UCC offers the potential to greatly improve aero-turbine engine performance through the combination of trapped vortex combustion and centrifugal force effects on combustion. Experimentally, variations of the UCC have been built and tested several times. The expense and time to run experimental tests limit the number of configurations that can be run. The experimental configurations also limit the amount of flow visualization that can be achieved due to construction. Further, the expense of constructing new models limit the number of tests that can be run in a real world set up. CFD work will greatly improve the optimization process by increasing the availability of internal flow visualizations while producing fast, inexpensive results.

The data from the recent experiments will be used to validate a numerical method of modeling the UCC. The CFD model based on the experimental configuration will be modified to investigate the amount of influence grid density and periodic boundaries play in the accuracy of the numerical model. After this has been investigated, the numerical model's geometric configuration was altered several ways and compared to the original numerical model using the Lefebvre parameters as well as the others that were specified above.

II. Background and Theory

2.1 Literature Review

2.1.1 Conventional Combustor Layout. Basic gas-turbine combustors usually consist of four main regions called the diffuser, primary zone, intermediate zone and dilution zone. These sections are seen in Figure 1. The description that pertains to the various sections of the typical combustor is detailed by Lefebvre [13] and is summarized below.

The diffuser's main purpose is to minimize the pressure loss across the combustor through the reduction of compressor outlet velocity. The pressure drop needs to be minimized for increased efficiency across the combustor. The diffuser also works to recover much of the dynamic pressure as well as providing a smooth stable flow for the liner. The liner then uses turbulence to increase the mixing for flame speed acceleration as the air moves into the other zones of the combustor.

The primary zone is the region of the combustor where the fuel is burned initially. Equivalence ratios (ϕ), or the actual fuel to air ratio compared to the stoichiometric fuel to air ratio [12], are generally higher in the primary zone. The primary zone is to provide a stable flame through the use recirculated flow. This recirculation of the hot combustion gases provide a region for stable, continuous ignition.

Downstream of the primary zone is the intermediate zone. Due to the high equivalence ratios found in the primary zone there are large amounts of Unburned Hydrocarbons (UHC) and CO that are formed in the primary zone. To decrease the

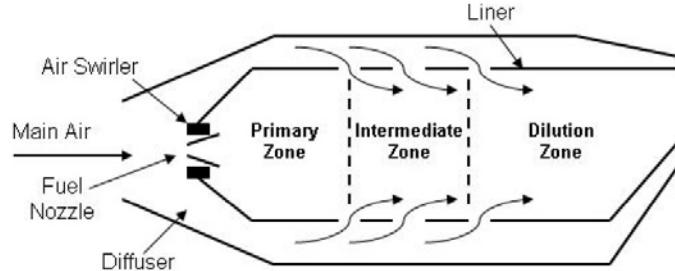


Figure 1: Typical gas turbine combustor configuration adapted from Lefebvre [13]

amount of these pollutants in the exhaust, the intermediate zone allows for the rich products to react with air from the diffuser for the UHC to burn and the CO to react with the oxygen. The added air also keeps temperatures down through the addition of non-combustion gases.

The dilution zone takes the remaining air from the diffuser and the products of combustion from the intermediate zone. This zone is used for the continued cooling of the combustion products as well as react any of the other secondary products and radicals that have resulted from the combustion of the earlier zones. This reduction in temperature and quenching of the radicals improves the lifespan of the turbine blades downstream of the combustor.

2.1.2 Trapped Vortex Combustion. The UCC is loosely based on the trapped vortex combustion. Aerodynamicists have tried to use and control vortex motion for possible benefits for years. Work done by Little and Whipkey [16] investigated the interaction of trapped vortices with drag and stability. Experiments were set up using a cylindrical forebody and an afterbody disc. The disc was placed at various distances downstream from the forebody to determine the minimum drag condition configuration. The distance between the disc and the cylindrical forebody was altered to change the dimensions of the cavity created between the two objects. Through flow visualization and LDV measurements they determined that if a cavity were dimensioned correctly, stable flow would fill the cavity and also produce a minimum drag condition. With X being the offset distance of the disc and D_0 being the diameter of the cylindrical forebody, they found that the proper dimensions for this stable vortex were at $X/D_0 \sim 0.6$.

Work done at the Air Force Research Laboratory (AFRL) used principles of the trapped vortices and attempted to achieve rapid mixing and vortex stability to improve combustion performance [22]. The AFRL researchers introduced a cavity of the same basic dimensions as Little and Whipkey to create a stable recirculation zone. One of these TVC setups can be seen in Figure 2. They ran experiments on

different configurations with operating pressures up to 15 atm and temperatures up to 850 K. They found that the TVC would offer many benefits resulting from the stable recirculation zone. Their research showed that the TVC offered improvements in Lean Burn Out (LBO), altitude relight, operating range, as well as a potential for decreased NO_x emissions compared to conventional swirl stabilized combustors. The lower NO_x levels are a benefit of RQL performance that are the result of the fast mixing between the fuel and the air associated with the stable vortical motion in the cavity [22].

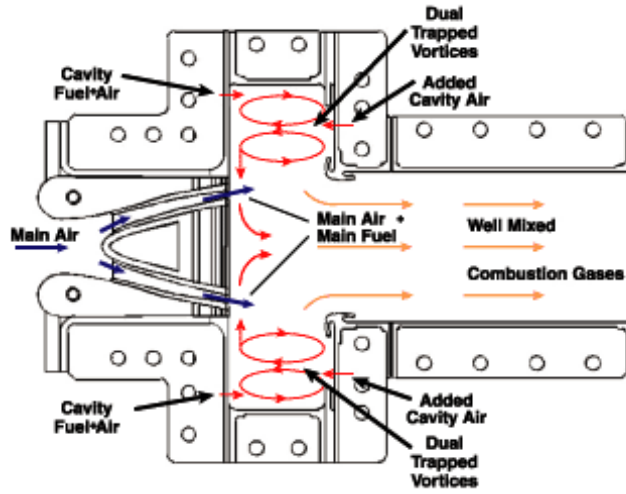


Figure 2: Trapped Vortex Combustion Concept Schematic [22]

2.1.3 Centrifugal Force Combustion. In an effort to increase flame propagation speeds, Lewis [15] experimented with high centrifugal force effects on combustion. Work was done on a combustion centrifuge, which essentially was a stainless steel pipe closed in at either end and spun around an axis of rotation. This apparatus was filled with a propane air mixture. Lewis [14] also ran tests with a hydrogen-air mixture. It was observed that below 200 g the flame speed (S_B) is independent of the g-loading. However, at centrifugal loadings above 500 g and up to 3500 g the flame speed increases in proportion to the square root of the centrifugal force as seen in Equation(1). This flame transport mechanism is known as “flame bubble transport” and is found to be significantly faster than both laminar and turbulent flame speeds.

$$S_B \propto \sqrt{g} \quad (1)$$

Yonezawa et al. [25] worked on improving the practicality of the high g-combustor by first running computational tests; then an experimental prototype was constructed from those numerical results. They were able to modify a typical combustor by introducing swirl through a series of air and fuel injections. These air injectors would be able to increase the circumferential velocities and thus increase the g-loading experienced. Yonezawa et al. were able to increase the loading while still producing higher combustion efficiencies than conventional combustor layouts. These tests showed that the fuel could be reacted at a faster rate; thus the length of the combustor could be decreased from typical layouts by up to 33%.

2.1.4 Inter Turbine Burner. In a typical aero-turbine engine, fuel is completely burned in the combustor before the resultant hot, high-pressure gas moves to the turbines. Sirignano and Liu [23] have shown that efficiency and specific thrust can be improved if the fuel continues to be burned through the turbines. That is to say, heat is added in the turbine where pressures are higher while work is done on the rotor. They have shown that this modified Brayton cycle can produce significant gains in specific thrust with only small increases in fuel consumption. Currently combustor and turbine materials prevent this constant temperature combustion from occurring. Rather than have a continuous burn in the turbine the stators can be converted into additional discrete combustors. An ITB would allow for another constant pressure heat addition which would translate into higher efficiencies and more power extraction without increasing the length of the entire combustor [17]. It has been shown that the ITB displays many of the same benefits of the continuous turbine burner, yet is presented in a more practical package. An image of this modified Brayton cycle is seen in Figure 3.

The possible applications and benefits for using an ITB are numerous. With the same weight of the engine, more thrust could be added with this reheat, thus

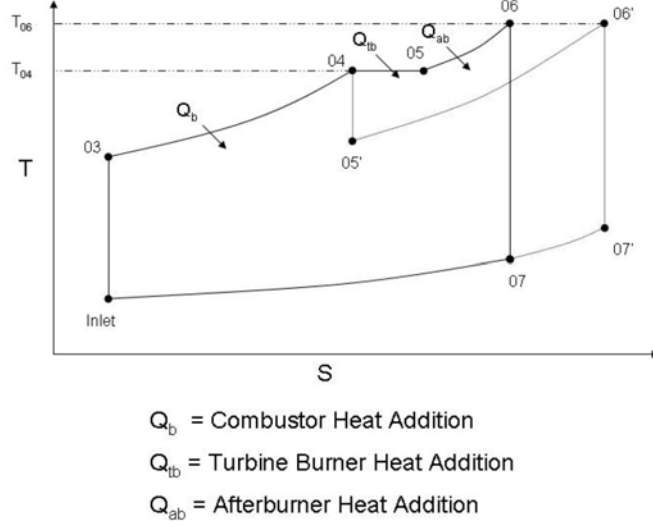


Figure 3: T-s Diagram for Conventional Combustor and ITB modified from Liu and Sirignano (Used without Permission) [17]

increasing the thrust to weight ratio. If the amount of energy imparted into each combustor were decreased, but keeping the total thrust the same, the maximum outlet temperatures would decrease. The lower temperatures would aid in increasing the mean time between maintenance. Conventional engines suffer from a loss of thrust when power is taken for shaft work. The addition of an ITB between the high and low pressure would mitigate the loss of thrust for power generation and provide more for thrust applications [26].

2.1.5 UCC. What is now known as the UCC is a result of the combination of the three previously mentioned combustion concepts. An image of a recent experimental setup of the UCC can be seen in Figure 4.

Anthenien et al. [2] set up atmospheric pressure experiments to test proof of concept for the ITB. They constructed a combustor with a cavity that ran around the circumference of the combustor. They were able to introduce swirl around the cavity to produce up to ~ 1000 g in this configuration. With tests run with both JP-8 and ethanol they were able to measure combustion efficiencies of over 99%.

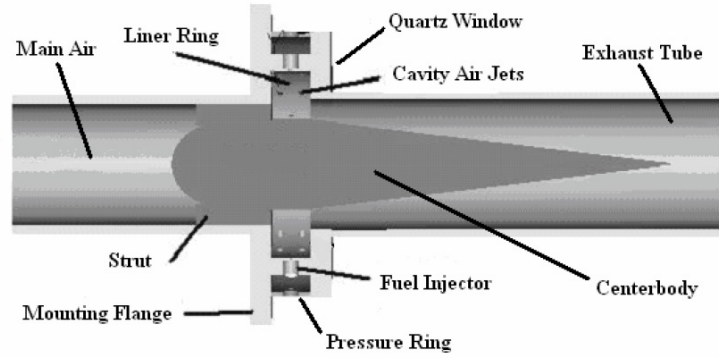


Figure 4: UCC Experimental Configuration Schematic [21]

Conceptually they determined that to drive the circumferential momentum in the cavity, the momentum could originate from the compressor or the upstream high-pressure turbine, depending on whether it is used the initial combustor or an ITB. With the combination of the stator and combustor, the UCC could be up to 66% shorter than the typical combustor configuration. An image of this conceptual layout is seen in Figure 5.

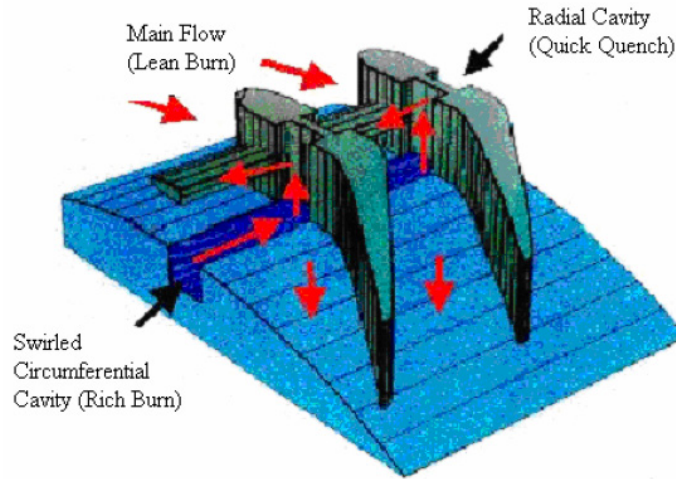


Figure 5: Integration of the UCC and Turning Vanes (Used with Permission from Anthenien et al. [2])

Further tests on the UCC were conducted following the atmospheric tests. Zelina et al. [26] varied the fuel injection method and angle in the cavity to optimize

the fuel injection process. In addition to the altered geometries they ran the experiments on high pressures and temperatures. These new conditions tend to change the behavior of the reaction.

In Zelina's experimental tests the flame lengths were shown to be 50% shorter than conventional combustors. Efficiencies were found to be 95% - 99% with a correlation between g-loading and combustion efficiency. These improvements came from higher flow density and improvements of fuel atomization for the experimental configuration.

Mawid et al. [18] conducted 3D numerical analysis of the UCC. They determined from CFD results that high efficiencies resulted from intense burning in a high g loaded cavity. They were able to show that the UCC was able to operate over a wide range of operating conditions. They determined that multiple combustion zones resulted from the air jets' penetration into the cavity. The radial vane was also shown to be effective in bringing hot combustion products down into the main flow from the cavity. To further improve the temperature profile at the exit, improved mixing is required between the cavity and the main flow.

Further experimental research by Quaale [21] indicate that the circumferential velocities were found to be 20 - 45 m/s in the cavity of the UCC, corresponding to g-loadings of 1000-4500 g. CFD work was also conducted in his study and showed comparable results to the experimental data that Quaale was able to obtain.

Most recently Greenwood conducted a numerical analysis of the UCC using Fluent. He observed that the size of the cavity had a large impact on the behavior of the flow. His work indicated that decreasing the length of the cavity by 20% reduced the pressure loss by 4-10%. His work also showed that small modifications of the model have large impacts on the efficiency and performance of the UCC [8].

2.2 *Computational Fluid Dynamics*

2.2.1 CFD History. With increasingly more powerful computers, the use of CFD has steadily grown since its start in the early 1970's when it was used for fairly simple flow problems. The major limitations to CFD are computational power and time required to solve a flow configuration [6]. As computational power has increased, the amount of flow conditions that CFD can simulate has also expanded and these limitations do not pose as large a problem as they once did.

2.2.2 Turbulence Modeling. In choosing a turbulence model it is important to choose a model that is both robust and accurate. There are many models from which to choose for the zero-order equations, such as the Baldwin-Lomax to higher order models like the $k - \epsilon$ and the $k - \omega$ models. The zero order equations are not generally used for complex flows due to the limited nature of how the turbulent viscosity is treated. The zero order equation treats the turbulent viscosity μ_t as seen in Equation (2), as a function of local flow properties and is not impacted by upstream mechanisms [1]. Introducing more sophisticated models is an attempt to introduce history effects into the calculation of the turbulent viscosity [5]. This is generally done by increasing the order of the solver. With successive equation models more partial differential equations are used to solve the flow parameters. The solution takes more computational time to compute when using increasing order equations so it is important to choose an appropriate model for the problem at hand that has sufficient accuracy for the desired flow but is not excessively computationally intensive.

$$\mu_t = \rho C_\mu \frac{k^2}{\epsilon} \quad (2)$$

$\mu_t = \text{Turbulent Viscosity}$

$k = \text{Turbulent Kinetic Energy}$

$\epsilon = \text{Turbulent Dissipation Rate}$

$C_\mu = \text{Fitting Constant}$

The $k - \epsilon$ has become the most common approach for typical engineering-type problems due to its robust nature and lower computational requirements. This model is one the simplest of the two-equation models. The $k - \epsilon$ model is based on solving the turbulent dissipation rate, ϵ , and the turbulent kinetic energy, k , simultaneously. These equations are seen in (3) and (4). The $k - \epsilon$ model is a good compromise between accuracy and computational effort [6].

$$\frac{\partial}{\partial t}(\rho k u_i) + \frac{\partial}{\partial x_i}(\rho k u_i) = \frac{\partial}{\partial x_j} \left[\left(\mu + \frac{\mu_t}{\sigma_k} \right) \frac{\partial k}{\partial x_j} \right] + G_k + G_b - \rho \epsilon - Y_M + S_k \quad (3)$$

$$\frac{\partial}{\partial t}(\rho \epsilon) + \frac{\partial}{\partial x_i}(\rho \epsilon u_i) = \frac{\partial}{\partial x_j} \left[\left(\mu + \frac{\mu_t}{\sigma_\epsilon} \right) \frac{\partial \epsilon}{\partial x_j} \right] + C_{1\epsilon} \frac{\epsilon}{k} (G_k + C_{3k} G_b) - C_{2\epsilon} \rho \frac{\epsilon^2}{k} + S_\epsilon \quad (4)$$

Another Fluent feature that was used to save computational time and space was to run the model steady. Running a steady solution requires far less time and less computational space. However the use of a steady solution will influence the accuracy of the solution. To ensure the CFD solution is acceptable the solution is compared to the experimental data and the accuracy of the model will be shown.

2.2.3 Wall Functions. Turbulent flow is characterized by irregular flow behavior that has flow properties on multiple length and time scales. To catch all the small eddies that are characteristic of turbulent flow the cell spacing would need

to be on the same order as the smallest scale. For practical engineering purposes this is not a realistic task. With many CFD tasks, such as airfoils and wind-tunnel comparisons, small cell sizes can be implemented to catch the specific areas of interest. An extremely dense mesh can be placed in these specific areas. With the UCC it is harder to catch the areas of interest with dense gridding because so much of the flow will be strongly influenced by turbulent behavior. Another method will need to be implemented to make the turbulent CFD modeling feasible.

For the full accuracy of a turbulent model there need to be many cells in the boundary layer to resolve the small vortices. A non-dimensionalized wall unit is defined in Equation 5 to help define the boundary layer characteristics. For turbulent flows, to put the first cell center within a y^+ of 1 the initial spacing for the UCC model would need to be much smaller than is practical. In addition to the initial spacing there would need to be many cells in the viscous sublayer ($y^+ < 5$). Rather than creating a grid with this many cells, this research will take advantage of the wall functions that Fluent has created to account for the relatively consistent nature of turbulent boundary layers [7].

$$y^+ \equiv \frac{U_\tau y}{\nu} \quad (5)$$

$y^+ = \textit{Turbulent Wall Unit}$

$U_\tau = \textit{Friction Velocity}$

$\nu = \textit{Kinematic Viscosity}$

In order for the wall functions to be accurate the grid size must be adapted for the flow. The wall functions work best if the center of the first node is in the log layer. The log layer is the region in the turbulent boundary layer that is between the viscous sub-layer and the outer region and has a logarithmic profile. This region corresponds to a y^+ of 30-300 [5] where y^+ is calculated using Equation (5). When gridding up the numerical model for turbulent flows using wall functions, Fluent recommends that

the y^+ should be on the low end of the log layer and should not be in the viscous sublayer or the buffer region between the viscous sublayer and the log layer. If the first cell is in the viscous sublayer the solution is assumed to be a linear boundary layer and is deemed inaccurate. However, the y^+ should be made to put the first cell near the lower bounds of the log layer to be most accurate [7].

The wall functions are used to make it more practical to track the turbulent flows without having to maintain the cell spacing to produce a proper turbulent boundary layer. The turbulent boundary layers are well modeled when the y^+ values are within the log layer, that is when the y^+ has been a major grid creation criteria. Through surface averaging in the CFD solver the models included in this presentation are all well within that realm with y^+ values of $\sim 30 - 100$.

2.2.4 Species Modeling. There are three primary ways to model chemical reactions in gas mixtures: frozen, rate controlled and equilibrium chemistry. Frozen flow reactions usually are so slow that their reaction has little effect on the mixture composition. This type is typically used for hypersonic flows because the residence times are much shorter than the time required to react. Rate controlled reactions are much more demanding for computational time. This form of reaction simulation evaluates how the mixture's composition changes with time. The third model is to assume the model has reached chemical equilibrium in each cell and time step. This reaction is rapid enough that the mixture state changes then reaches an equilibrium. It is also known as a mixed-is-reacted model in that the oxidizer and fuel quantities are calculated and when proper equivalence ratios are found in the cell a reaction occurs. This model is far less computationally expensive and is valid as long as the reaction time is significantly shorter than the residence time [9]. The mixing time, or the ratio of turbulent kinetic energy to turbulent dissipation rate, was found to vary from 0.14 ms to 0.50 ms in the models included. The mixing time is therefore about an order of magnitude greater than the chemical time. For this research the chemical

time is of the order of $50\mu s$. Since the mixing time is about an order of magnitude greater than the reaction time, the equilibrium solver can be used.

The UCC is modeled with non-premixed combustion in Fluent. Non-Premixed combustion occurs when fuel and air enter a system as two independent quantities, as opposed to premixed combustion that has the fuel and the oxidizer enter the system already mixed. Fluent [7] then calculates the mixture fraction, f , for each cell. The mixture fraction is the mass percentage of fuel in a gaseous mixture, essentially the mass of material having its origins in the fuel stream to the mass of the mixture [12]. The mixture fraction is defined in Equation (6). The reactions then become a mixing problem based on the probability density function (PDF) that is contained in the Fluent software for the given operating conditions and loadings.

$$f = \frac{Z_i - Z_{i,OX}}{Z_{i,fuel} - Z_{i,OX}} \quad (6)$$

2.2.5 Emissions. The emissions of an engine disclose much about the efficiency and performance of the reaction that occurred. The largest portion of the exhaust is composed of carbon dioxide (CO_2), water (H_2O), oxygen (O_2) and nitrogen (N_2). There are other species that result in much smaller levels that cause greater concern to the environment. These include carbon monoxide (CO), unburned hydrocarbons (UHC) and oxides of nitrogen (NO_x).

The amount of unburned fuel that escapes a combustor is a concern of combustor designs. Liquid fuel hitting the turbine blade can cause wear and, more importantly, any unburned hydrocarbon, be it vapor or liquid, is a waste in efficiency and is also considered a pollutant. To calculate the unburned hydrocarbons both the liquid and vapor phases of the hydrocarbons are included.

Carbon monoxide can be fatal if inhaled in sufficient quantities. It is created in a fundamental step in the combustion process; however, most of it will react with the excess O_2 to form CO_2 with complete combustion. CO that does not react with the O_2 is an indicator of lost efficiency. Carbon monoxide can usually be removed

by high temperatures and increased residence time but this solution brings about another harmful emissions species, NO_x [13].

2.2.6 NO_x Modeling. NO_x is an important parameter to be able to model. As was previously emphasized, lowering the amount of NO_x produced in a given engine is an important task for engine designers. Three mechanisms can produce oxides of nitrogen: fuel, prompt and thermal. Fuel NO_x is generally in heavy fuels like diesel where its production can be significant, but for aeronautical purposes is generally not as important [13].

Prompt NO_x is produced quickly at the flame front. The exact mechanisms that produce the prompt NO_x are not well understood, but Lefebvre [13] asserts the enhanced reaction rates come about from the intermediate reactions produced during the main hydrocarbon reactions.

Thermal NO_x is produced by oxidation of N_2 with post flame gases and is found in the high temperature regions of the reaction. It is generally taken that the formation of the Thermal NO_x is a result of the extended Zeldovich mechanisms given in three principal reactions seen in Equations (7-9) from Kuo [12].



Some fuels contain higher amounts of organically-bonded nitrogen. If the fuel contains this nitrogen it can then produce fuel NO_x in which N bound in the fuel is oxidized directly. The amount of fuel NO_x that is released is dependent on the combustion process. Light distillate fuels contain 0.06% nitrogen where heavy distillates contain up to 1.8% nitrogen. Depending on the nitrogen conversion the fuel NO can represent a significant portion of the NO released [13].

NO_2 is formed when the NO from the exhaust relaxes with the oxygen and ultraviolet light in the atmosphere to become NO_2 . NO_2 is a primary component of smog which creates air quality problems in many major cities [13].

2.2.7 Post Processing. To calculate the four Lefebvre parameters of interest, combustion efficiency, temperature pattern at the exit, emissions and pressure loss, CFD post-processing methods will be used. In order to use this data with certainty it is important to investigate how Fluent calculates this data.

Species data is looked at on a mole basis to determine the efficiency and behavior of the internal flow. The experimental data to which the numerical UCC will be compared to is mainly exhaust samples. Fluent has different methods of calculating the properties of the exiting gas to help match the values. Two major ways to get data are mass and area weighted averaging. Mass weighted averaging, which is calculated using Equation 10, will be used in this research [7]. This method of averaging results is used because it gives stronger weighting to the faster moving species from the center of the flow.

$$\frac{\int \phi \rho |\vec{v} \cdot d\vec{A}|}{\int \rho |\vec{v} \cdot d\vec{A}|} = \frac{\sum_{i=1}^n \phi_i \rho_i |\vec{v}_i \cdot \vec{A}_i|}{\sum_{i=1}^n \rho_i |\vec{v}_i \cdot \vec{A}_i|} \quad (10)$$

2.3 Heat Transfer

Combustors are often assumed to be adiabatic at the boundaries. However, to more closely match the experimental results heat loss will be modeled on most of the boundaries in the numerical model of the UCC. To model the heat losses radiative and convective heat transfer were included on the model surfaces. Convective losses were calculated following the explanation of Incropera and DeWitt [11] on the convective heat loss of horizontal cylinders.

To determine the heat transfer coefficient two relationships for Nusselt Number, \bar{N}_{uD} , are equated to form Equation 11. The convective heat transfer coefficient, \bar{h} , is

solved for where D is the diameter of the combustor in m and k is a function of the surface conditions. The Prandtl number, Pr , is assumed to be 0.7 for the air.

This analysis of the convective heat transfer on a horizontal cylinder needs to be accomplished in order to set up appropriate heat transfer coefficients for the various boundaries conditions of the UCC in the numerical model.

$$\bar{N}_{uD} \equiv \frac{\bar{h}D}{k} = \left[0.60 + \frac{0.387Ra_D^{1/6}}{[1 + (0.559/Pr)^{9/16}]^{8/27}} \right]^2 \quad (11)$$

The Rayleigh number used in Equation (11) is defined in Equation (12) also from Incropera and DeWitt [11]. The scalars are g , or the acceleration due to gravity, ν is the kinematic viscosity T_∞ and T_s are freestream and surface temperature respectively.

$$Ra = \frac{g\beta(T_s - T_\infty)x^3}{\nu\alpha} \quad (12)$$

2.4 Pattern and Profile Factors

Two parameters are designed to quantify the exit plane's temperature spread and location: pattern and profile factor. The pattern factor is calculated using Equation 13. The mass weighted average of temperature on the inlet and exit plane are used as well as the maximum temperature on the exit plane. This parameter is difficult to assess experimentally due to the limited temperature information that can be determined from experimental probes. Lefebvre [13] asserts that the lifespan of the nozzle guide vane and the turbine blades are highly dependent on the temperature distribution of the combustor exit.

$$PatternFactor = \frac{T_{4_{max}} - T_{4_{avg}}}{T_{4_{avg}} - T_3} \quad (13)$$

$T_{4_{max}}$ = *Maximum Outlet Temperature*

T_3 = *Mean Inlet Air Temperature*

T_4 = *Mean Exit Temperature*

The profile factor as seen in Equation 14 looks at the maximum mean circumferential temperature of a radial location (T_{mr}). It is this value, T_{mr} , that is of most importance to the turbine blade lifetime. This mean radial temperature is obtained by averaging the temperatures for the various radial heights [13].

$$ProfileFactor = \frac{T_{mr} - T_4}{T_4 - T_3} \quad (14)$$

The ideal temperature distribution for the combustor exit would be uniform for the pattern and profile factor. Thus the ideal pattern and profile factor would be zero. To reduce the pattern and profile factor the maximum T_4 and T_{mr} need to be as close to the average exit plane temperature as possible.

III. Methodology

3.1 Experimental Results for Validation

Experiments have been conducted at high pressures by Zelina et al. at Wright Patterson AFB with a small scale UCC. The tests were run using a variety of loading conditions. These loading conditions used various temperatures, pressures and mass flow rates for both the cavity and the main inlet. Also, to show the combustor's wide operating range, the equivalence ratios were varied as well.

Results from some of these tests were selected for comparison to the CFD model. The selected loading conditions are shown below in Table (1). The five operating conditions use the naming convention where LM, MM and HM denotes low, medium and high mass flow rates respectively. The LP, MAP, and HP represent the low, moderate and high pressure conditions respectively. The Combustor Loading Parameter (CLP) is defined in Equation (15). In Equation (15) \dot{m}_{cav} is in kg/sec, V is in ft^3 , P_{T_3} is in $psia$ and T_3 is in Rankine for the below equation [8].

$$CLP = \frac{\dot{m}_{cav}}{\frac{P_{T_3}}{14.7}^{1.75} V e^{\frac{T_3}{540}}} \quad (15)$$

This parameter is used to be able to compare different loading conditions on different geometries as well as among other geometries. The CLP may be viewed roughly as an inverse residence time giving the fuel less time to react as CLP is increased.

Table 1: Experimental Loading Conditions

	\dot{m}_{main} $\frac{kg}{min}$	\dot{m}_{cavity} $\frac{kg}{min}$	P (psia)	$\frac{dP}{P}$ (%)	T_3 K	$\phi_{overall}$	ϕ_{cav}	CLP
Case1 (LMHP)	13.2	2.9	41.2	4.7	491	0.29	1.62	0.68
Case2 (LMMP)	13.5	2.8	49.4	3.0	515	0.29	1.68	0.46
Case3 (HMHP)	29.5	5.8	59.2	8.2	530	0.15	0.90	0.66
Case4 (MMHP)	23.0	5.5	62.3	4.9	475	0.17	0.89	0.64
Case5 (LMHP)	13.4	3.5	61.1	2.8	526	0.34	1.62	0.39

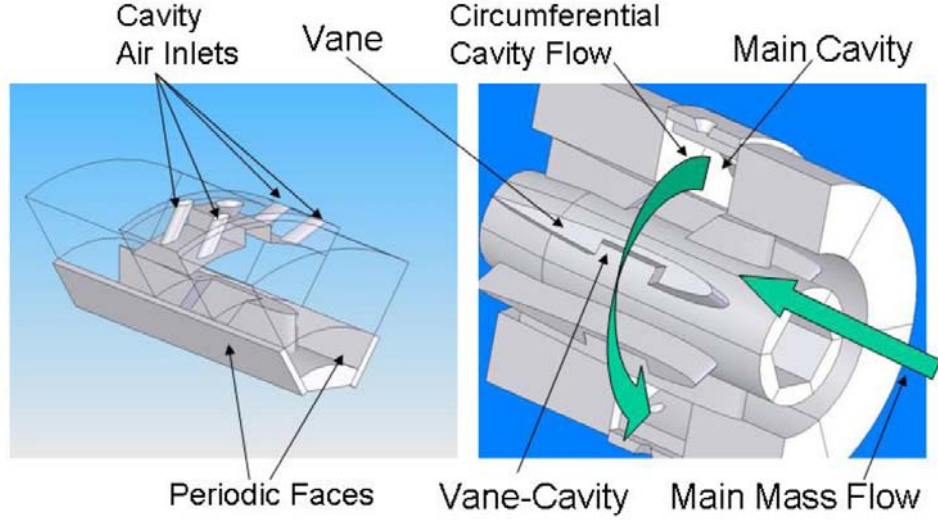


Figure 6: Two views of the UCC configuration

Around the circumference of the cavity were 12 pairs of air-inlets. The inlets had a radius of 2.7 mm and were located 20° from the fuel injection locations. These air inlets were canted off the radial to impart the circumferential momentum around the cavity that is so essential for the high-g combustion. Experimentally the cavity had a length of 47.6 mm and a vane height of 13.7mm. A view of the periodic section can be seen on the left hand side of Figure 6 and the full UCC on the right hand side of Figure 6.

The fuel used for these experiments was JP-8+100, a kerosene based fuel. Fuel was injected into the model at six equally spaced locations around the circumference of the cavity in an axially recessed cavity. The fuel was injected using a pressure-atomizing nozzle yielding a Sauter mean diameter of approximately 55 microns, a flow number of 0.5 for each of the six injectors and a half cone angle of 35° . The Sauter mean diameter of a fuel droplet is defined in Lefebvre [13] as the droplet diameter that has the same surface to volume ratio as the entire fuel injection spray.

In the experimental rig, four probes were inserted into the flow downstream of the vane's trailing edge. The results from the four different probes for CO , CO_2 , O_2 , NO_x and unburned hydrocarbons were averaged. At both the inlet and the outlet

temperature and pressure data were obtained from two locations on the circumference of the combustor and averaged.

3.2 Numerical Methods

Two different general methods have been used to numerically model the UCC in this research. In the first method, the UCC has been segmented into six equal periodic sections. Periodic faces have been used to greatly reduce the number of cells needed to run a configuration. Each $1/6^{th}$ slice of the UCC has a vane, one fuel injection point and four cavity air inlets and $1/6^{th}$ of the total air from the main inlet annulus. This periodic model geometry can be seen in greater detail in Figure (7). In the second method, the UCC has been modeled using the entire combustor. The entire UCC was constructed by placing six of the periodic sections together to complete the entire combustor. This was implemented to validate the use of the periodic section for the CFD analysis.

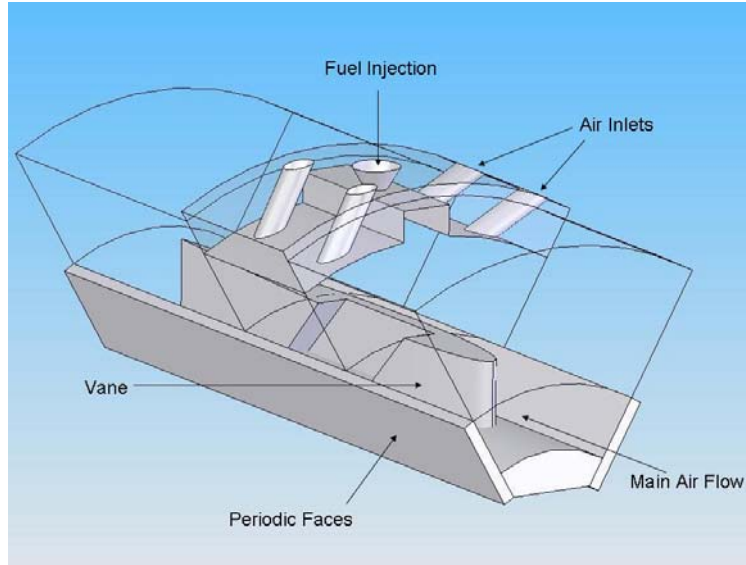


Figure 7: Periodic Section of the UCC

Fluent 6.2 was the CFD program on which the numerical models were tested. The solver used was a segregated model on a steady $k - \epsilon$ turbulent model. Non-

premixed combustion was used. The chemical modeling included 11 species with a steady state solution.

3.2.1 Grid Development. All models were produced in Solidworks. It then converted the particular geometry into an initial graphics exchange specification (IGES) file. Gridgen then converted the IGES into a frame to build a mesh. On that frame a 3D unstructured mesh was created. In Gridgen the boundary conditions were assigned and then converted to a Fluent case file where the flow could be developed and analyzed [20].

Six additional geometries were investigated. The first modification was to shorten the cavity in the axial direction to 38.1 mm from 47.6 mm. The second modification shortened the cavity's length further to 25.4 mm. On this cavity layout the angle of the air injections was increased twice from 37° to 45° and further to 55° . The fifth modification was to improve the aerodynamics of the vane cavity and introduce holes in the leading edge of the vane which lead to the vane cavity. The last modification was to increase the height of the vane to 25.4 mm with the base cavity configuration. Many different cavity configurations were looked at in the scaling up of the vane height. It was decided to match the CLP of the baseline model while using the same mass fluxes for all the air inlets. The air inlet areas were therefore increased by 24% on the tall vane model. The fuel mass flow rate also had to be increased by the same percentage to match the equivalence ratios in the cavity. The specifics of all the modifications are found in Table (2).

Table 2: Numerical Models

	Cavity Length (<i>mm</i>)	Inlet Angle (deg)	Vane Height (<i>mm</i>)	$D_{AirInlets}$ (<i>mm</i>)	# of Cells
Baseline	38.1	37	13.7	5.33	395,000
Inch 37	25.4	37	13.7	5.33	358,000
Inch 45	25.4	45	13.7	5.33	364,000
Inch 55	25.4	55	13.7	5.33	352,000
Nozzle	38.1	37	13.7	5.33	638,000
Tall Vane	38.1	37	25.4	6.02	597,000

3.2.2 Discrete Phase Model. The fuel is tracked using Discrete Phase Model (DPM). The droplets trajectories are tracked through the combustor after it is injected from the five cones of the fuel injector. The DPM's mass is tracked separately from the vapor, however as the injected fuel evaporates that mass is included with the rest of the mass in the combustor.

To model the reaction of the fuel to the walls of the UCC Fluent offers several possible reactions. A wall jet boundary condition is used in this research. The wall jet boundary condition in Fluent uses the impingement angle (ϕ) and the Weber number to produce the resulting momentum flux. The wall jet boundary condition assumes an analogy with an inviscid jet impacting a solid wall [7].

3.2.3 Fuel Injections. To model the fuel injections in Fluent a DPM method is used. Five hollow cones were set up using various half cone angles and droplet diameters to model the distribution of a typical fuel injector. They were injected into the model at 30.5 m/s. The liquid fuel is modeled as kerosene because of kerosene's similar thermodynamic properties to that of JP-8+100. Vaporized fuel was modeled as $C_{12}H_{23}$. The fuel was radially injected from an axially recessed cavity situated on the outer circumference of the cavity into the model at 300K.

To model the fuel injector five hollow mono-disperse cones were overlayed. The five cones vary in half cone angle from $30 - 40^\circ$ and the droplet mean diameter varies from $40 - 70\mu m$. The specifications of the cone model are found in Table (3) [8]. This variation in fuel droplet size is needed because not all droplets will be the same diameter in a test experiment [3]. Since fuel evaporation is highly dependent on surface area and droplet size, a spread of droplet sizes is required to better match the experimental data.

3.2.4 Species Modeling. The PDF was set up in Fluent to include 11 species for all the cases. An equilibrium solver was used due to its computational efficiency and reasonable accuracy. This method is commonly known as mixed-is-reacted. A

Table 3: Fuel Injection Model

Cone #	Mean Diameter (μm)	Mass Flow (%)	Half Cone Angle (deg)
1	40	10	40
2	50	25	30
3	55	30	35
4	60	25	32
5	70	10	38

PDF was created for each of the case's loading conditions. The species included O_2 , N_2 , $C_{12}H_{23}$, CH_4 , CO_2 , CO , H_2 , H_2O , $H_2O(liquid)$, OH and $C(solid)$.

To calculate the amount of a species in the exhaust of the flow a mass averaged mole fraction was taken at the exit plane. This method was done for the CO , CO_2 , O_2 and NO_x . For the UHCs a different method needed to be used. The mole fraction of $C_{12}H_{23}$ taken at the exhaust represents only the vapor form of the fuel. It is found in much lower magnitudes than other species because the equilibrium solver reacts most of the fuel vapor upon evaporation and little is left in the exhaust. In addition to the small amount of kerosene vapor at the exit plane, the liquid fuel is not included in these species results because its flow characteristics are tracked using the separate DPM system. To get an accurate value for the UHC the vapor mole fraction is added to the ratio of fluid concentration over the hydrocarbon's molar mass to the sum of that with the average density of the exhaust over the exhausts molar mass. How the unburned fuel is calculated is more easily seen in Equation (16).

$$ppm_{HC} = ppm_{vapor} + \frac{\frac{\rho_{HC}}{MM_{HC}}}{\frac{\rho_{exhaust}}{MM_{exhaust}} + \frac{\rho_{HC}}{MM_{HC}}} \quad (16)$$

Directly linked to the PDF creation is the specification of an operating pressure, (P_{OP}). The PDF is created using various parameters but the operating pressure that the CFD model uses is linked to the way the species are reacted and thus becomes the basis for how many of the other flow parameters are calculated.

3.2.5 Pollutant Process Modeling. Of the three NO_x models that can be calculated in Fluent, only Thermal and Prompt NO_x will be modeled and the Fuel NO_x will not be included. The omission of fuel NO_x may lower the amount of the pollutant calculated at the exit plane but as previously stated this mechanism does not produce NO_x in as large an amount as the other two mechanisms. In Fluent NO_x will be included in with the other species calculations and the mass weighted molar fraction will be used to obtain the specific values of the pollutant. Fluent calculates only the NO in the calculation of NO_x . This assumption can be made because the amount of NO is about 50 times greater than NO_2 at the exit of the combustor for typical JP-8 fuels [9].

3.2.6 Boundary Conditions. Boundary Conditions are used to closely simulate the real world flow and material conditions. CFD is somewhat limited in that all flow properties can not be set because the flow will become overconstrained. This occurs when too many parameters are defined. Therefore it is necessary to let some variables float and select the more important ones to define.

For the model air inlets, the main annulus inlet and the cavity inlets, a mass flow boundary condition was chosen. This boundary condition was chosen to control the equivalence ratios in the cavity and the main flow. The selection of this inlet condition will cause the pressure at the inlets to float to the numerical solution.

The outlet was taken to be a pressure outlet. The importance of the pressure of the high temperature and pressure loadings made it essential to specify this parameter rather than use a simple outlet. The outlet backflow temperature was set to be near the assumed adiabatic flame temperature for the equivalence ratio of the particular loading conditions.

The vane and the centerbody were modeled as adiabatic. This assumption is made due to the combustor's symmetry. The top of the cavity was defined as a convective surface in which the emissivity, ϵ , was set to 0.85. Experimentally a plenum of 535 K air surrounded the cavity. The freestream temperature was thus set

to 500K to simulate the experimental conditions. The cavity flanges were set to be a mixed radiative and convective surface with an emissivity, ϵ , of 0.85. The freestream temperatures for these walls were taken to be 300 K. The flanges and the top of the cavity had a heat transfer coefficient of $8.1 \frac{W}{m^2K}$.

The inlet outlet walls were assumed to be the mixed convective and radiative heat transfer with the 0.85 emissivity. The inlet wall was given a heat transfer coefficient of $10.2 \frac{W}{m^2K}$ and the exit wall was given a heat transfer coefficient of $12.1 \frac{W}{m^2K}$. These values for the heat transfer coefficients were initially calculated by Greenwood [8] using Equations (11-12).

Since all six sections were identical periodic sections could be applied. Therefore for the periodic wedge cases the sides are defined as rotationally periodic where the periodic planes bisect the vanes axially. The CFD package will treat these opposing periodic boundaries as if they were adjoining planes and transfer the flow conditions to the opposite periodic plane. [7]

3.2.7 Convergence Criteria. The use of numerical methods requires a discussion of solution convergence. The residuals, or the flux imbalances, of the solution are calculated with successive iterations and are driven down until convergence is reached. Convergence of a solution can be defined in many ways. The default for Fluent defines convergence when the continuity and velocity components of the residuals reach 1E-3; energy is converged at 1E-6, which means that three and six orders of residual reduction occur for the respective components. However, with complicated flow conditions as are modeled here, this level of convergence is seldom achieved. Another way of determining if a solution is converged is if the residuals plateau out and successive iterations do not decrease the magnitude of residuals. This implies that a solution is reached and this can be considered converged.

A combination of these two methods was used for this research. The model was computed until the residuals leveled out. If all the residuals for the given model did not reach 1E-3 the relaxation parameters were used to try to force the residuals lower.

These parameters can speed up a solution and cause the residuals to drop; however, the residual behavior becomes oscillatory and unstable. Finding the proper mix of relaxation parameters needed to reduce the residuals and damp out the oscillations is not an exact science and divergence of the solution can occur if the wrong set of relaxation parameters is applied.

3.3 Comparison Criteria

3.3.1 Combustion Efficiency. The efficiency is a relation of the of the maximum possible energy that could have been released during the combustion process to the amount of energy actually released [19]. In a experimental setup it is difficult to determine the total amount of heat released but a relation of the amount of *CO* and UHC in the exhaust can be used to calculate the efficiencies. It has been discussed that the *CO* is an incomplete combustion by-product and the UHC are a sign of further incomplete combustion, so this relation is a practical way to determine the efficiency.

The efficiency of the combustor is calculated using Equation (17) here H_C is the heat of combustion for the fuel and (EI) is the emissions index for the species and is defined by Equation (18). For kerosene, H_C is approximately $43,500 \frac{kJ}{kg}$ [4]. The emissions index is calculated using Equation 18. The emissions indices also serve as a good parameter to compare the amount of pollutant produced for different combustors. For the numerical model with the increased vane height the EI serves as a better comparison tool than the ppm values because of the increased fuel flow in the model. The EI can compare the amount of pollutant produced for the particular amount of fuel injected into the combustor.

$$\eta_b = 100 \left[1.00 - 10100 \frac{EI_{CO}}{H_C} - \frac{EI_{C_{12}H_{23}}}{1000} \right] \quad (17)$$

$$EI = \frac{g_{pollutant}}{kg_{fuel}} \quad (18)$$

Since Fluent is using an equilibrium solver, the modeling of a slow reaction like CO is not done as accurate as possible. The combustion efficiency is entirely calculated using emissions data, therefore the calculated efficiencies will depend strongly on these elevated equilibrium results.

3.3.2 Pressure Drop. The pressure drop that occurs in a combustor is also tied to the efficiency of the engine. The pressure drop is a way to quantify the losses associated with the combustor's design and combustion process. The calculated pressure drop is defined in Equation (19). The pressure losses associated with combustors are comprised of two main components that can be broken down into hot and cold pressure losses. Although not actually a loss in efficiency, the hot pressure drop comes from the bulk acceleration of the hot gases as the density decreases from the internal reaction. The cold losses come from friction on the combustor walls [10]. The pressure loss term is a method to quantify the combination of terms in a way that combines the losses and gives an overall amount of the combined losses. It should be noted that, experimentally, this value was set by controlling the back pressure of the combustor. Here the pressure loss is looked at as an efficiency parameter because in the numerical model the inlet pressure floats for the given solution.

$$\frac{dP}{P} \% = 100 * \frac{P_3 - P_4}{P_3} \quad (19)$$

3.3.3 G-Loading. Since flame speed is related to the centrifugal acceleration it is important to see the effect that the cavity length and grid model have on the average circumferential velocities. Average circumferential velocities, U_θ have been calculated by introducing a vertical plane and taking the mass-weighted average of the velocity component.

$$g = \frac{U_\theta^2}{g_0 R} \quad (20)$$

The g-loading term that is so important in the flame propagation values is calculated using the aforementioned U_θ term included in Equation (20). As the g-loading is related to R, or distance from axis of rotation, with increasing this value the circumferential velocities will need to be scaled up to maintain the same level of g-loading.

3.3.4 Periodic Boundaries. The periodic boundary is an instrumental tool that is used to save computational time. If the model uses repeating geometry a periodic boundary can be used. The model is segmented into identical pieces and the model treats these opposing periodic boundaries as if they were adjoining planes and transfer the flow conditions to the opposite periodic plane. The periodic boundaries can be used to transfer DPM properties across the boundary as well [7].

IV. Results and Discussion

4.1 *Validation of the CFD Model*

Validation of the CFD model was achieved by comparing results from a computational UCC model to experimental data. The UCC was modeled three ways to show that neither the grid density nor the use of periodic boundaries played a significant role in the accuracy of the numerical models.

The first model was constructed with a fairly coarse grid density on the experimental UCC configuration using the periodic boundaries discussed earlier. A denser grid was then constructed using the same periodic geometry only with the additional number of cells. These models were run on the same flow conditions. The denser grid had approximately four times the number of cells than the original model. This additional model was constructed to illustrate that the grid density does not improve the accuracy of the model enough to warrant the extremely dense mesh. Then, to show that the periodic boundaries did not play a significant role in the accuracy of the model, the five other periodic sections were placed together to create a full UCC. In the Fluent manual there is mention of conflicts with the use of periodic sections in conjunction with the DPM model for fuel. The three models were run on the first loading condition, LMLP, as defined in Table1. Table4 compares the three CFD cases to the experimental data using some of the various combustion parameters discussed earlier.

4.1.1 Comparison. The CFD models compare well to the experimental data. The data from the three runs shows that with the successive assumptions the accuracy of the model diminishes only slightly. The full model is closest to the experimental on most of the parameters listed above. The *CO* levels are elevated for the three numerical modelling techniques, with the coarse model being $\sim 30\%$ elevated over the experimental values. The elevation of the *CO* in the exhaust was expected and comes from the use of the equilibrium solver. The fact that all three models show signs

Table 4: Validation Data for Coarse, Dense and Experimental

	Coarse	Dense	Full	Experimental
$CO(ppm)$	1454	1389	1220	1089
$CO_2(\%)$	3.8	3.7	3.7	3.2
$O_2(\%)$	14.8	15.0	15.0	16.4
$NO_x(ppm)$	39.8	42.1	40.0	37.3
$UHC(ppm)$	92.4	85.8	107	100
$\eta_b(\%)$	95.6	95.9	95.4	97.5
$\frac{dP}{P}(\%)$	5.9	5.8	5.9	5.0
Pattern Factor	1.0	1.0	1.1	-
Profile Factor	0.29	0.36	0.31	-
U_θ (m/s)	27.6	28.5	25.5	-
# Cells	376,000	1,123,000	2,258,000	-

of similarly elevated CO levels further supports the equilibrium chemistry assumption reacting more of the fuel and air.

The CO_2 values in the exhaust are an indication as to the extent of the combustion process. As the CO_2 increases and the O_2 decreases, more of the fuel is reacting with the oxidizer in the combustor. With the equilibrium solver and the lean limit defined in the PDF function, the numerical model indicates through the resulting species data that the combustor is reacting more of the fuel than would physically happen. With the data in Table 4 it is seen that the CO_2 is only $\sim 15\%$ elevated compared to the experimental data. The O_2 is on average $\sim 10\%$ lower than the experimental data. Together these parameters also indicate that the model is reacting more of the fuel.

The NO_x process is one of the least understood methods that is numerically modeled and previous numerical tests have shown difficulties calculating accurate values for the NO_x . The above table shows that the three grid methods all calculate the NO_x within 15% of experimental data. The coarse model, whose approximate grid density will be used for this research, shows a good relation to the experimental data on this parameter.

Efficiency of the combustor is related in two separate ways. The combustion efficiency is the metric used to quantify the amount of energy that is released from the fuel, whereas the pressure loss quantifies the hot and cold losses that the combustor imparts on the flow. The combustion efficiency is slightly lower in all the numerical models. This reduction is mainly attributed to the $\sim 30\%$ increase in CO from the use of the equilibrium solver. The amount of UHC in the exhaust are well modeled and indicate that the numerical model produces data that is within 15% of the experimental data.

The other method of calculating efficiency involves the pressure loss across the combustor. As was discussed earlier, this calculated pressure loss comes from two different components. The total pressure loss value combines the hot and cold losses which gives an overall indication of the total losses. The models all show greater pressure loss terms and the increase was approximately 20%. The higher pressure loss may come from the numerical model reacting more of the fuel in the main cavity which would increase the hot losses or it may also include increased cold losses related to the use of wall functions.

The circumferential velocities Quaale [21] observed were between 20 and 50 m/s. The values that were calculated in the cavity of the numerical models all lie well between those parameters as they range from 25.5-27.6 m/s. The layout of the combustor used in these experiments was slightly different from Quaale's. However, the magnitude of the velocities calculated in this research show that the CFD is still able to produce appropriate values for the circumferential velocities.

4.1.2 Pattern and Profile. Experimentally the pattern and profile factors were not calculated, so they will be used to compare the different numerical models created. Below in Figure 8 is an image of temperature contours on the exit plane. The hot spot is located just left of the midline of the image. The hot spot results from the hot combustion gases that travelled from the main cavity into the vane cavity. From the vane cavity these gases exited into the main channel and traveled downstream

with the main flow. The hot gases exiting the vane cavity stayed radially out in the combustor which results in the corresponding regions of higher temperatures on the exit plane near the top of the exit plane. The right side of the pressure outlet has much lower temperatures. The temperatures on the right side of the exit plane midline resulted from the inability of the main air flow to mix effectively with the cavity combustion gases. It can be seen that the hot combustion gases need to be brought down lower on the exit plane to create a more uniform temperature distribution.

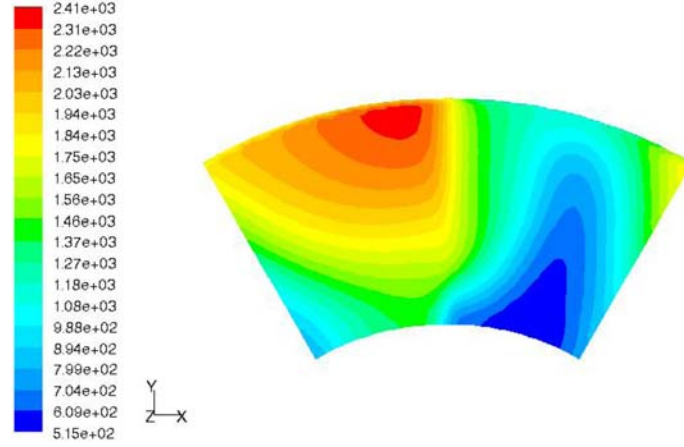


Figure 8: Temperature Contours on the Coarse Model with LMLP Loading Condition at the Exit Plane

In Table 4 the pattern and profile data are included. These two values are important in improving the MTBM for the downstream turbine blades so decreasing these values is an essential task in combustor design. The values for these two parameters are within 10%-20% between the three models. The similarities between the full UCC and the periodic sections, especially on these parameters, indicate that the three grid methods produce similar results.

Investigating the temperature profiles at the exit plane as is seen in Figure 9 is also important in improving the life of the turbine blades. This figure is created by calculating the average circumferential temperatures for the distribution of radial values on the exit plane. These temperatures were plotted against a non-dimensional radial value from zero to one. Lefebvre [13] indicates that the ideal temperature distri-

bution would be uniform. This distribution would appear as a vertical line on this plot having a constant temperature for all the radial values. Since a uniform temperature distribution was not observed, the maximum mean circumferential temperature was found by locating the maximum temperature over the span of non-dimensionalized radial values on this plot.

In comparing the three model configurations, it is observed that the average radial temperatures are consistent. The maximum mean radial temperatures for the coarse model and the full model are within 5% all of which are occurring in the top 5% of the non-dimensionalized radial location. These three profiles show that there is a large spread of mean radial temperatures, ranging from 900K-1750K on the radial which indicates the need for improvement by providing a more uniform temperature distribution.

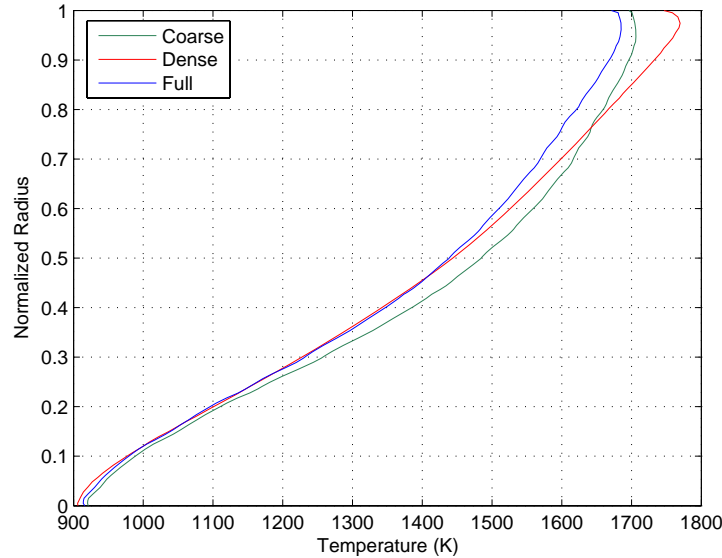


Figure 9: Average Circumferential Temperatures at the Exit Plane for the Coarse, Dense and Full UCC Models on LMLP

The full UCC showed the best correlation to experimental data and the dense periodic section provided slightly better results than the coarse model. However, the minimal improvement in accuracy was not worth the extra computing time that is associated with the extra cells of the two other configurations. The future modifica-

tions of the UCC geometry were conducted on a model of comparable grid density to that of the coarse model. With the model validated against the experimental data the geometric modifications were examined.

4.2 Base Model

Previous research conducted by Greenwood showed that the reduction in cavity length improves the performance of the combustor [8]. He observed that the decreased length improved the pressure loss from 4-10% with only a small increase in harmful pollutant emissions. The other advantage of the model is that the smaller cavity translates to smaller engine components by reducing the size and volume of the combustor.

The numerical model was changed from the experimental geometry slightly. The length of the cavity is reduced by 9.5mm split equally on both sides. The location of the fuel injector and air inlets remained fixed with respect to each other, thus air inlets are closer to the walls of the cavity. It was determined that the decreased distance from the wall did not increase the wall shear significantly. This configuration will be considered the baseline and will be the standard against which the other modifications are compared.

Table 5: Species and Efficiency Data for the Baseline Model Compared to the Coarse Model Data

	$CO(ppm)$	$NO_x(ppm)$	$CO_2(\%)$	$O_2(\%)$	$UHC(ppm)$	$\eta_b(\%)$	$\frac{dP}{P}\%$
Coarse-1	1454	39.8	3.8	14.8	92	95.6	5.9
Baseline-1	1148	38.5	3.8	14.9	111	95.4	5.6
Coarse-2	1499	53.2	3.8	14.9	62	96.4	3.8
Baseline-2	1335	55.6	3.7	15.0	74	96.2	3.6
Coarse-3	285	12.1	1.8	18.2	31	97.3	8.6
Baseline-3	284	10.7	1.8	18.1	33	97.2	7.9
Coarse-4	321	15.4	2.2	17.5	32	97.8	5.1
Baseline-4	366	14.1	2.3	17.4	36	97.5	5.0
Coarse-5	2192	98.2	4.5	13.9	28	97.0	2.9
Baseline-5	2044	90.9	4.4	13.9	39	96.9	2.7

4.2.1 Species and Efficiency. The baseline model was compared to the coarse model from the above validation study. The coarse model was run on the other four loading conditions to compare to the shorter cavity model. Although previous work was done using this 38.1 mm cavity configuration, needed modifications were made to the numerical method in construction of the periodic boundaries. This required the model to be rerun on the selected loading conditions.

The data indicates there is a general reduction in CO and NO_x in the exhaust, for the same amount of CO_2 produced. This reduction is seen in Table 5 on four of the five loading conditions for both the CO and NO_x . These emissions trends differ from previous work in that it was found that the harmful emissions increased slightly with this configuration [8].

The shorter cavity increased the amount of UHC on the exit plane. This is due to the radial velocity increase on the shorter cavity, pushing more of the unburned fuel droplets into the main channel. This increase of UHC in the exhaust is the cause of the reduced combustion efficiency compared to the experimental model. Pressure loss reductions are also seen in all the loading cases. The pressure loss likely stems from the fact that the flow appears to be better contained in the main cavity. This reduced pressure loss follows the trend Greenwood observed on this shorter cavity model.

4.2.2 Internal Flow Investigation. Figures 10 and 11 show velocity vectors colored by temperature on two different planes on the LMLP loading condition. The vectors in Figure 11 show that the higher temperature gases are occupying the lower portions of the main cavity. As the high swirl flows over the vane much of the hotter gases move down into the vane cavity. It is seen that a clear vortex is created there on the back side of the vane. Figure 10 shows the perpendicular view of this phenomenon. It is seen that there are hot gases that fill the middle of the main cavity between the two air inlets indicating that the main cavity flow is better controlled. As the hot

gases come over the vane it can be seen that they fill the vane cavity almost completely and move out downstream towards the pressure outlet.

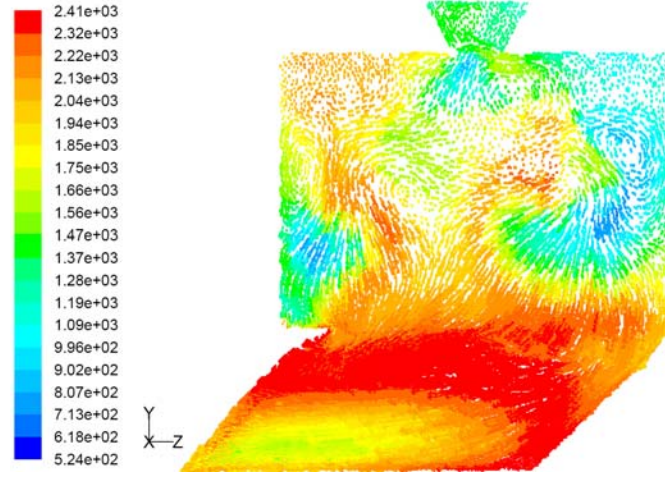


Figure 10: Velocity Vectors colored by Static Temperature on the Radial Plane Midline Plane for Baseline Model on LMLP Loading Conditions

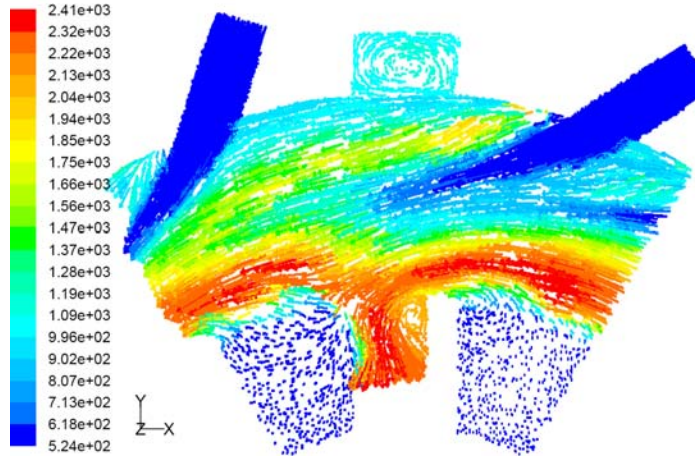


Figure 11: Velocity Vectors Colored by Temperature on Same Axial Plane with Front Air Inlet of Baseline Model for LMLP Loading Condition

4.2.3 Pattern and Profile. The mean circumferential temperatures are seen in Figure 12. The five loading conditions show that there is a variety of mean circumferential temperature behaviors at the exit plane. On the HMHP loading condition the base model has a smaller spread for temperatures on the exit plane. The difference between the maximum and minimum temperatures is only 400 K. In addition

to improvements in temperature uniformity the increased cavity loadings also reduce the T_{mr} . With the higher loading conditions, in addition to the higher cavity mass flow, there is also an increase in main air flow. The increased main airflow is decreasing these exit temperatures compared to the lower loading conditions even though there is additional fuel and air added to the cavity in the higher loading conditions. When compared to the coarse model, the maximum mean radial temperature on the LMLP loading is higher in the baseline model. This translates to a higher profile factor which is also seen on all the other loading conditions as well. Table 6 shows the calculated data for the pattern and profile factors. Although the pattern factor shows mixed results for the different loading conditions, the profile factor is higher than the experimental model for all cases.

Table 6: Pattern and Profile Data for Baseline compared to the Coarse Model Data

	$T_{4avg}(K)$	$T_{mr}(K)$	Pattern Factor	Profile Factor
Coarse-1	1172	1706	1.00	0.29
Baseline-1	1153	1741	0.91	0.34
Coarse-2	1173	1713	0.99	0.28
Baseline-2	1155	1768	0.93	0.34
Coarse-3	868	1109	0.99	0.18
Baseline-3	869	1160	1.14	0.27
Coarse-4	913	1184	0.99	0.21
Baseline-4	925	1218	0.99	0.24
Coarse-5	1298	1936	0.88	0.37
Baseline-5	1262	1879	0.83	0.36

To qualitatively gauge the pattern factor, the temperature contours on the exit plane are investigated. The flow appears to have two separate temperature lobes. These lobes can be seen in Figure 13. As the flow is swirling in a counterclockwise motion, as looking down the main inlet of the combustor, it can be seen that the higher temperatures lie on the leeward side of the vane. The hot gases that leave the vane cavity stay fairly high in the main flow channel. The exit plane image shows this clearly with the hot temperatures left of the midline and high up on the exit plane. The flow on the other side of the midline does not seem to be as well mixed with the exit plane temperatures remaining largely below 1000 K. The maximum temperature

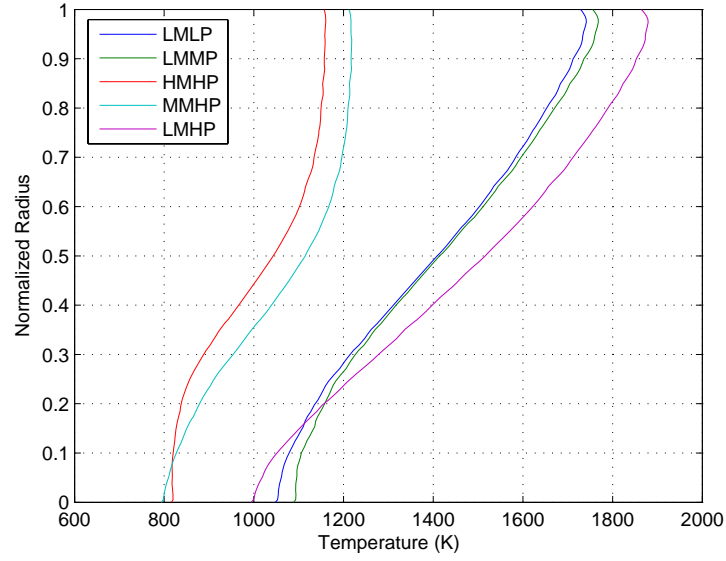


Figure 12: Average Circumferential Temperatures at the Exit Plane for the Baseline Model on the Five Loading Conditions

in this image is reduced compared to the experimental configuration as was seen in Figure 8. This reduction in temperature is also seen in the reduced pattern factor (Table 6) for the lower loading conditions. The higher loading conditions do not show this reduction compared to the experimental model.

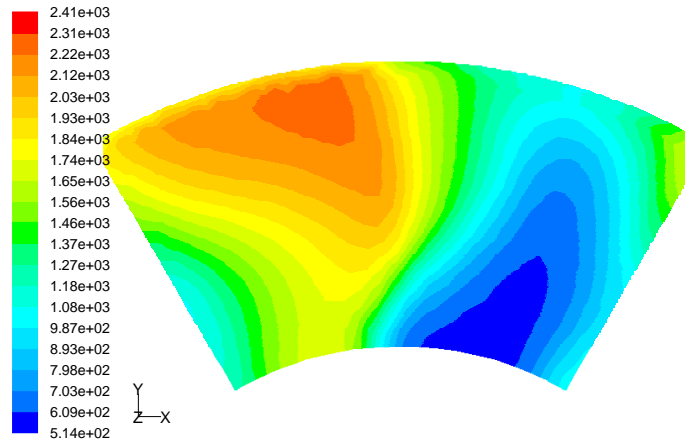


Figure 13: Temperature Contours on the Baseline Model with LMLP Loading Condition at the Exit Plane

4.3 Shortened Cavity Model

Further shortening of the cavity was conducted to investigate if the baseline cavity is still too large. In Figure 10 it is seen that areas of cooler flow occur mainly in the upper front corner of the cavity. A shorter model was investigated. The cavity has been shrunk to a total length of 25.4 mm. The air inlets were kept in the same position in relation to the cavity. In modifying this shorter model the fuel injection location was held constant, but the air inlets needed to be moved inward so as not to interfere with the cavity walls. Their locations were at 20% and 80% of the axial length of the cavity which correspond to 5.1 mm and 20.3 mm.

4.3.1 Species and Efficiency. The species data indicates that shrinking the cavity reduces the harmful emissions produced by the combustor as seen in Table 7. The CO emissions are down in all the loading cases and their reductions range from 3% to 20%. The NO_x is reduced in three of the five loading conditions. The two loading conditions in which the cavity saw the increases in NO_x production had CLPs of 1.3, about twice the combustor loading of the original numerical model. The higher loadings also relate to the lower cavity equivalence ratios. The loading parameter was increased by this significant number due to the volume of the shorter cavity being about 1/2 the size of the experimental configuration which corresponds to a near doubling of CLP.

Table 7: Species and Efficiency Data for the Inch37 Model Compared to the Baseline Model Data

	$CO(ppm)$	$NO_x(ppm)$	$CO_2(\%)$	$O_2(\%)$	$UHC(ppm)$	$\eta_b(\%)$	$\frac{dP}{P}\%$
Baseline-1	1148	38.5	3.8	14.9	111	95.4	5.6
InchCav-1	1032	30.0	3.7	15.0	182	93.4	5.9
Baseline-2	1335	55.6	3.7	15.0	74	96.2	3.6
InchCav-2	1083	41.4	3.7	15.0	119	95.1	3.8
Baseline-3	284	10.7	1.8	18.1	33	97.2	7.9
InchCav-3	276	18.6	1.8	18.2	46	96.3	8.0
Baseline-4	366	14.1	2.3	17.4	36	97.5	5.0
InchCav-4	346	26.1	2.3	17.4	56	96.5	5.2
Baseline-5	2044	90.9	4.4	13.9	39	96.9	2.7
InchCav-5	1607	65.9	4.4	13.9	76	96.4	2.9

It is again observed that the amount of UHC have increased with the shorter cavity. This value has increased by $\sim 80\%$ compared to the original configuration. With the cavity length reduced in size, the radial velocity increases again. This increase in radial velocity pushes more of the fuel out into the main flow to react in the main channel. The cold losses also increased with the shorter cavity. The air inlets were situated closer to the wall which increased the amount of drag the high circumferential velocities and air inlets will produce.

The pressure loss increased slightly on all five loading conditions in this shortest cavity. The increases in pressure loss are all below 10%; but with the reductions in harmful emissions the model shows improvements.

4.3.2 Internal Flow Investigation. Inside the flow the same behavior is seen as is found in the baseline model. In Figure 14 the hot gases are filling the cavity more completely than the baseline model. Two of the air inlet streams can be seen in the interior of the cavity. The hot gases are separated by the lower temperature air inlets. In the region above the air inlets, the flow is nearly normal to the plane. This is seen by the small profile of the velocity vector and the result is high circumferential velocities. Below the cavity air inlets the flow is less normal to the vertical plane. The air inlets appear to be introducing swirl into the flow as the flow comes over the top of the vane cavity. In addition to the swirl, the air inlets appear to be assisting in pushing the flow of the hot combustion gases over the vane into the vane cavity.

The image looking down the inlet of the UCC also shows the cavity being largely filled with hot gases. In Figure 15 the velocity vectors colored by temperature show the cavity flow coming over the vane. Similar to the baseline model, there is a region of hot gases at the same radial location. This radial location corresponds to the area where the main channel flow meets the cavity flow and potentially comes from the rich products of the cavity reacting with the air of the main flow and completes the reaction of some CO and some UHC.

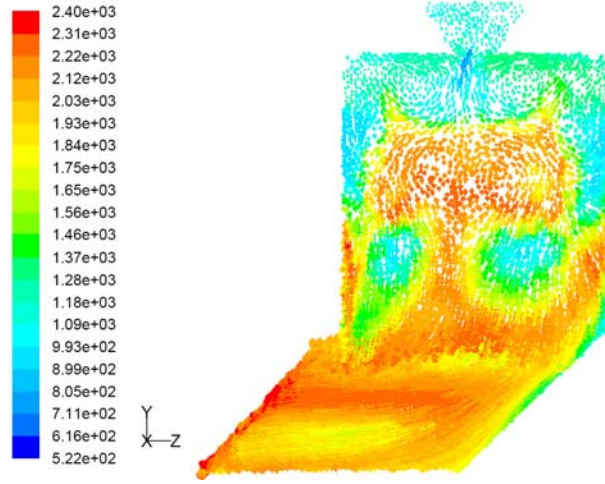


Figure 14: Velocity Contours Colored by Temperature on Same Axial Plane with Front Air Inlet of Inch37 Model for LMLP Loading Condition

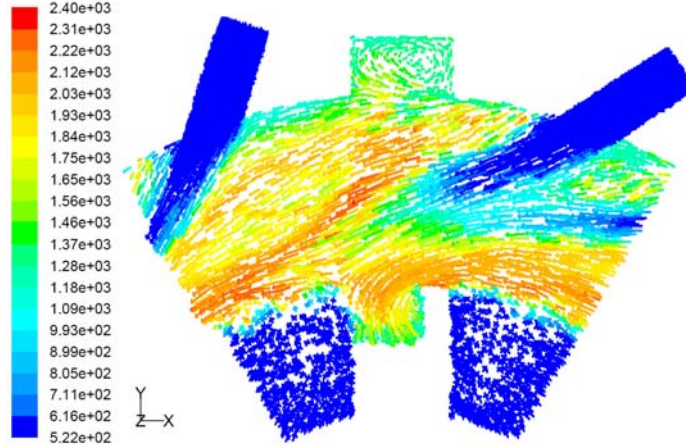


Figure 15: Velocity Vectors Colored by Temperature on same axial Location as the Front Air inlets of the Inch Cavity Model

4.3.3 Pattern and Profiles. The pattern and profile factors show higher values compared to the baseline model as seen in Table 8. While the pattern factor increases only slightly for the shortened cavity, the profile factor has increased greatly. The average temperatures on the exit plane are not significantly different, indicating that the increase in profile factor can mostly be accounted for by higher maximum mean circumferential temperature coming from the hot gases spreading out on the same radial values as opposed to travelling radially down into the flow.

Table 8: Pattern and Profile Data for Inch37 compared to the Baseline Model Data

	$T_{4avg}(K)$	$T_{mr}(K)$	Pattern Factor	Profile Factor
Baseline-1	1153	1741	0.91	0.34
Inch37-1	1154	1825	1.08	0.54
Baseline-2	1155	1768	0.93	0.34
Inch37-2	1157	1868	1.11	0.58
Baseline-3	869	1160	1.14	0.27
Inch37-3	864	1293	1.32	0.71
Baseline-4	925	1218	0.99	0.24
Inch37-4	918	1410	1.12	0.66
Baseline-5	1262	1879	0.83	0.36
Inch37-5	1265	2031	0.86	0.57

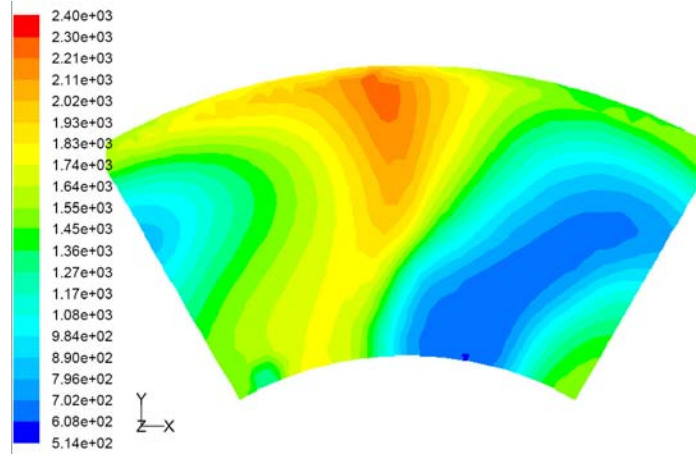


Figure 16: Temperature Contours on the Inch37 Model with LMLP Loading Condition at the Exit Plane

The profile factor is much larger with the shorter cavity model. The highest temperature gases stay at higher radial values in the UCC and do not have the temperature spread that was seen in the baseline profile comparisons. The profile comparisons in Figure 17 show that the mean circumferential temperatures are constant from 0 to about 70% of the non-dimensionalized radius. From the 70% radial location out, the average radial temperature increases sharply. The shape of the profiles is consistent for the five loading conditions, unlike the baseline models that had rather different profile behaviors. The hot gases that stay at high radial values are also seen in Figure 16. This image of the LMLP loading condition shows that the

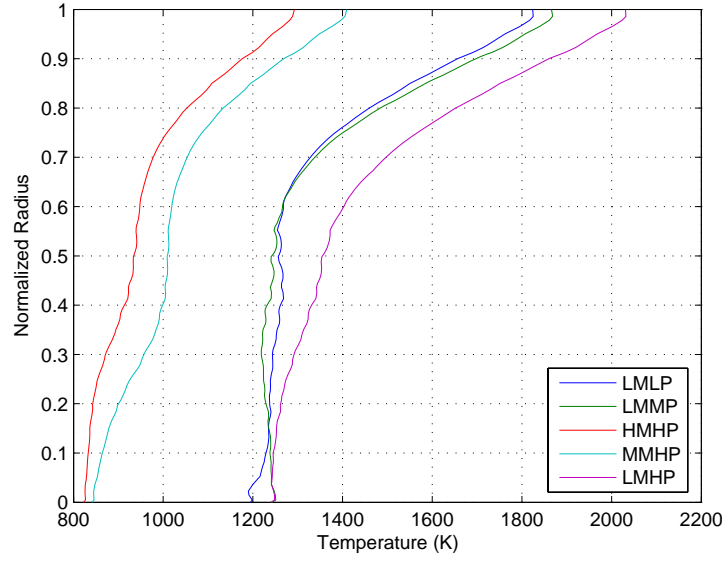


Figure 17: Average Circumferential Temperatures at the Exit Plane for the Inch37 Model on the Five Loading Conditions

temperatures at lower radial values are fairly constant. Out in the highest portions of the exit plane the temperatures increase with the hottest temperatures located near the midline of the exit plane.

4.4 Increased Air Injection Angle Models

As seen in the previous model, the one inch cavity model was more effectively filling the cavity volume with hot gases than the two longer cavity models. However, this model also produced higher UHC at the exit plane. To try to keep the fuel in the cavity longer, while possibly keeping more high temperature gas in the cavity, the angle of the air injections was increased from 37° to 45° and further to 55° . This increase in inlet angle will reduce the radial velocities and put more of the air inlet momentum into increasing the circumferential velocities that lead to higher flame propagation speeds.

4.4.1 Species and Efficiency. The species data for the three air inlet models are compared in Table 9. It is seen that the 45° air inlets produce the least CO

of the three inlet angle models for the same CO_2 . However, the 55° model shows benefits in terms of reducing the amount of NO_x produced and limiting the amount of UHC found at the exit plane. The reduction of CO and UHC have shown the 55° model operates at the highest efficiency of the three inlet angle schemes over the given operating conditions. The increased amounts of UHC at the exit plane on the lower loading conditions are surprising for the 45° case. For these loading conditions, this model produced the highest amount of the UHC of the three air inlet models. This could be the result of the lower temperatures in the cavity, which would reduce the evaporation rate of the droplets in the cavity. The increased angle of the air inlets will increase the circumferential momentum of the cavity flow. The residence time of the fuel in the cavity will therefore be increased. The added residence time should give the fuel more time to evaporate and for that evaporated vapor to react as is seen consistently on the third and fourth loading conditions.

Table 9: Species and Efficiency Data for the Inch37 Model Compared to the Inch45 and Inch55 Model Data

	$CO(ppm)$	$NO_x(ppm)$	$CO_2(\%)$	$O_2(\%)$	$UHC(ppm)$	$\eta_b(\%)$	$\frac{dP}{P}\%$
Inch37-1	1032	30.0	3.7	15.0	182	93.4	5.9
Inch45-1	863	25.5	3.7	15.1	204	93.0	5.8
Inch55-1	964	22.5	3.7	15.0	149	94.5	6.0
Inch37-2	1083	41.4	3.7	15.0	119	95.1	3.8
Inch45-2	956	35.5	3.6	15.2	147	94.5	3.8
Inch55-2	923	33.1	3.7	15.0	103	95.8	3.8
Inch37-3	276	18.6	1.8	18.2	46	96.3	8.0
Inch45-3	259	14.3	1.7	18.2	32	97.3	8.3
Inch55-3	288	8.2	1.8	18.1	6	98.8	8.6
Inch37-4	346	26.1	2.3	17.4	56	96.5	5.2
Inch45-4	319	16.2	2.3	17.4	48	97.0	5.5
Inch55-4	368	14.2	2.3	17.3	10	98.8	5.6
Inch37-5	1607	65.9	4.4	13.9	76	96.4	2.9
Inch45-5	1372	68.6	4.4	13.9	79	96.6	2.9
Inch55-5	1574	68.5	4.4	13.9	48	97.2	3.0

An increased pressure loss is observed with higher air inlet angles in Table 9. As the angle increases the flow gets faster near the upper surfaces in the cavity. Faster flow near the surface of the cavity will result in higher drag forces. The shorter cavity

model also has the air inlets closer to the cavity walls which will increase the drag as was seen with the 37° model. These higher drag forces will increase the cold losses in the cavity, leading to overall pressure loss increases.

4.4.2 Internal Flow Investigation. Figure 18 shows a much different flow structure than the 37° model. The initial shorter cavity model indicated that much more of the cavity volume was occupied by hot combustion gases. This model looks as though more of the hot flow is pushed down into the main airflow. In the 37° model the air inlet's jets are visible but the mixing of the hot gases is occurring both above and below these jets. In the 45° and also in the 55° model the hot gases are occupying only the region below the air inlets. The air inlets aid in separating the hot gases from the cooler gases near the walls of the cavity. This highly stratified temperature distribution could be resulting in the interesting behavior of the UHC in the models on the lower loading conditions.

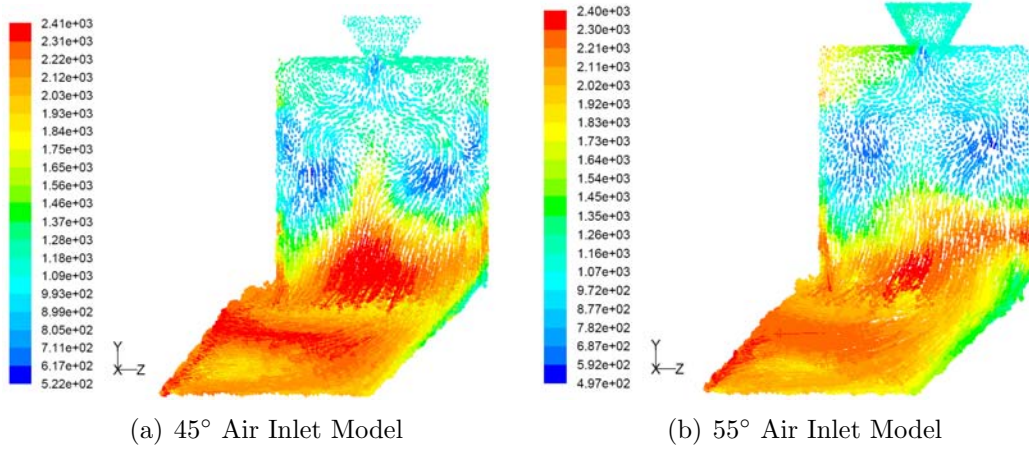


Figure 18: Velocity Vectors Colored by Temperature on Same Axial Plane with Front Air Inlet of Inch45 and Inch55 Model for LMLP Loading Condition

In Figure 19 it can be observed that the hot gases are only residing in the region just above the vane on the same radial location. It appears that the angle increase has caused a stronger temperature gradient in the cavity, causing the hot products to remain on the edge of the cavity and the main airflow. The 45° and the 55° models

display the same boundary of hot gases with the 55° model showing a much steepened temperature gradient.

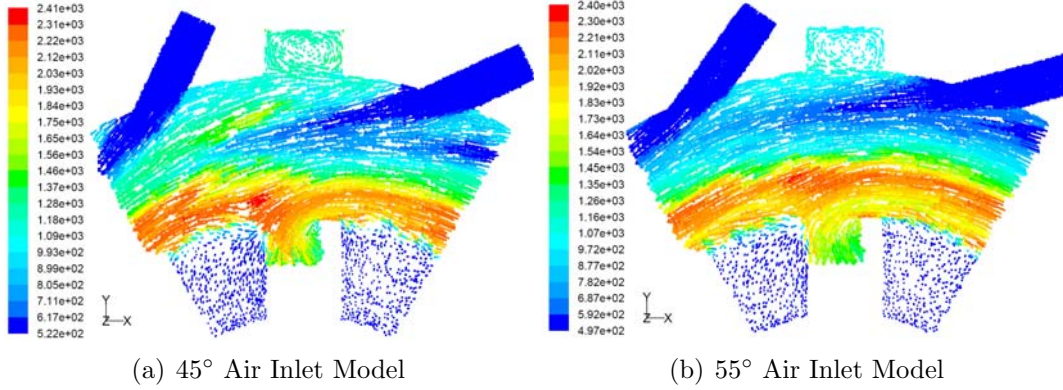


Figure 19: Front Air Inlet Velocity Contours Colored by Temperature for Shorter Cavity Models

4.4.3 Pattern And Profile. The outlet temperature contours for the increased inlet angles are similar to the 25.4 mm cavity model with 37° cavity air inlets. As seen in Table 10, the 45° inlet scheme produces the lowest profile factors of the three inlet models. This can also be seen in Figure 20. The dotted lines represent the mean circumferential temperatures of the 55° model and the solid lines represent the 45° . At lower radial values on the exit plane the higher inlet angle schemes have lower mean radial temperatures for all loading cases. Towards the top of the combustor at about midheight the 45° model's mean circumferential temperatures become lower than the higher angle model. Thus, the 45° model for each loading case has the lowest maximum mean circumferential temperature which corresponds to the best, lowest profile factor.

The outlet temperature contours on the LMLP loading condition are seen in Figure 21. The contours appear to be nearly identical to those seen in the 37° model in that there is a near uniform distribution up to the 0.75 radial location and then increases greatly near the top of the exit plane. The average surface temperatures are slightly lower in the 45° model. While the profile factor indicates that 45° model is best for the downstream turbine blade the pattern factor does not correlate as well.

Table 10: Pattern and Profile Data for Inch37 compared to the Inch45 and Inch55 Model Data

	$T_{4avg}(K)$	$T_{mr}(K)$	Pattern Factor	Profile Factor
Inch37-1	1154	1825	1.08	0.54
Inch45-1	1141	1742	1.04	0.45
Inch55-1	1146	1824	0.97	0.52
Inch37-2	1157	1868	1.11	0.58
Inch45-2	1144	1868	1.11	0.58
Inch55-2	1154	1825	1.08	0.54
Inch37-3	864	1293	1.32	0.71
Inch45-3	860	1193	1.37	0.44
Inch55-3	873	1230	1.54	0.54
Inch37-4	918	1410	1.12	0.66
Inch45-4	920	1329	1.17	0.43
Inch55-4	931	1363	1.27	0.54
Inch37-5	1265	2031	0.86	0.57
Inch45-5	1267	1903	0.82	0.39
Inch55-5	1260	1991	0.76	0.46

The highest cavity loadings, loadings 3 and 4, show that the increased cavity loadings worsen the pattern factor. Whereas the lower loading factors show that higher angles for the air inlets decrease the pattern factor slightly.

The 45° and 55° models have the air added to the cavity with less radial momentum. This reduction in radial momentum comes from the trade off that was used to keep the fuel in the cavity longer with the higher circumferential momentum. This trade off results in less momentum driving the cavity flow into the main flow. This results in the high mean circumferential temperatures near the top of the exit plane which could explain the increased profile factor in the 55° air inlet model.

4.4.4 Fuel Particle Tracks. The main motivation in the increasing the angle of the air inlets was to increase the fuel droplet's residence time inside the cavity. To investigate the benefits of the increased air inlet angles, particle tracks of the fuel droplets were used to visualize the response of the higher angle models. Below in Figure 22 are the particle tracks of the fuel in the cavity on the 37° air inlet model. It can be seen that the fuel is crossing the periodic boundaries and coming in the other

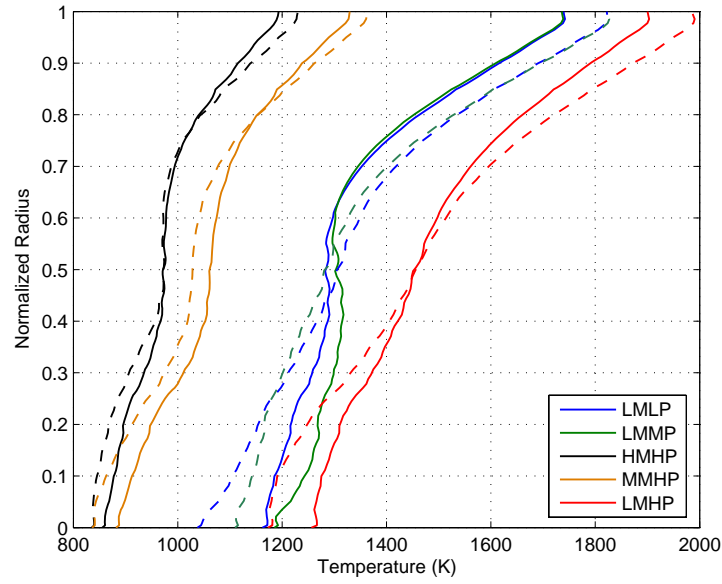


Figure 20: Average Circumferential Temperatures at the Exit Plane for the Inch45 and Inch55 Model on the Five Loading Conditions. The Dotted Lines represent the 55° Model and the Solid Lines Represent the 45° Model

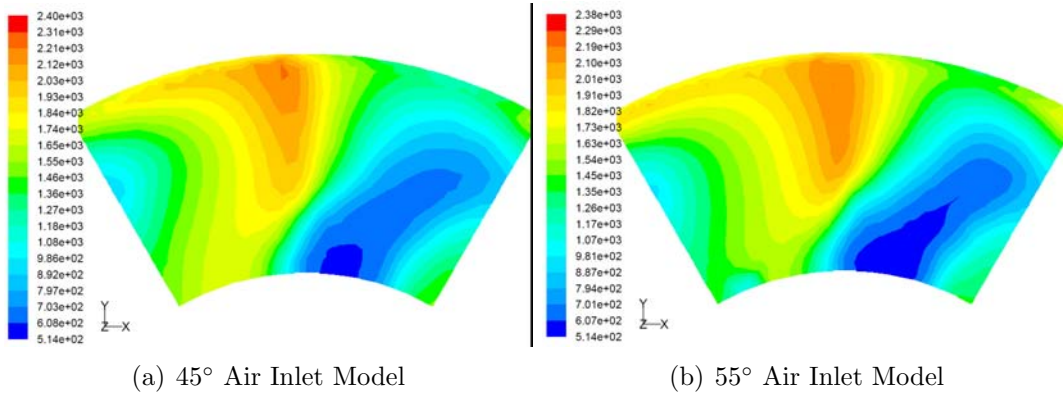


Figure 21: Temperature Contours on the Inch45 and Inch55 Models with LMLP Loading Condition at the Exit Plane

side freely. This calms concerns about conflicts between the discrete phase model and the periodic boundaries. Fluent tracked the number of particles escaping the exit plane to be ~ 500 fuel particles of the 1250 that were tracked in the liquid form on the HMHP loading condition.

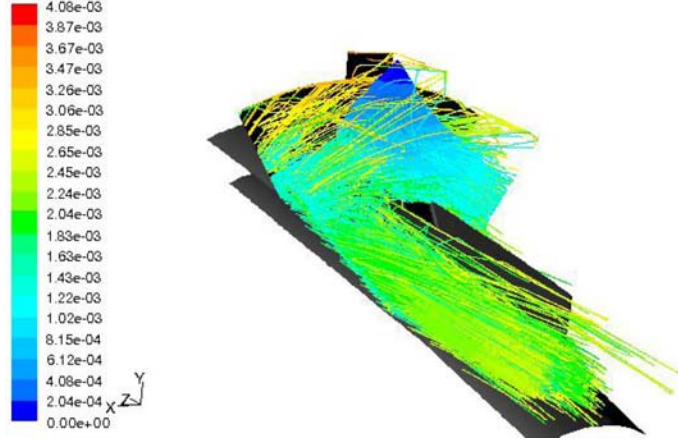


Figure 22: Fuel Particle Tracks on One Inch Cavity model with 37° air inlets. Lines are Colored by Residence Time

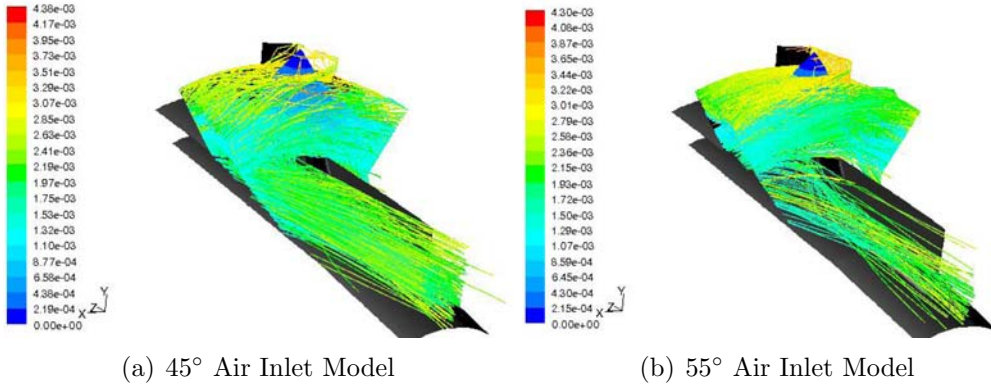


Figure 23: Fuel Particle Tracks on Shorter Cavity Model with Increased air Inlets Angles. Lines are Colored by Residence Time

When increasing the angle of the air inlets it is observed that the fuel stays in the cavity longer as seen in Figure 23. On the 45° model, the cavity is filled with the fuel traces and the number of fuel particles exiting the combustor has fallen to ~ 275 from the 1250 that are tracked from the fuel injector. The 55° inlets showed the fuel staying in the cavity the longest with only ~ 50 droplets escaping the combustor in liquid form. This increase in fuel droplet residence time in the cavity can be seen in the HMHP loading case where the UHC has decreased to six ppm from 33 ppm of the baseline configuration with that loading.

4.5 *Aerodynamically improved Vane*

The vane in the combustor has been modified to improve the aerodynamics as well as to include inlets in the leading edge of the vane. There are five inlets that have been introduced in the leading edge of the vane to transport mass from the main flow into the vane cavity. These inlets have the same area on the vane cavity side of the holes. However, on the leading edge of the vane the holes vary in size in that the area of the lowest hole is twice the area of the top hole. With twice the mass flow and the same exit area, the velocity of the air coming out of the bottom most hole is twice that of the top hole. This difference in velocity helps bring down mass by producing lower pressures near the bottom of the vane cavity. This pressure gradient aids in lowering the hot cavity mass in the vane cavity and reducing the profile factor at the exit plane downstream. The vane cavity was also aerodynamically improved by smoothing out its aft corner. The smoother aft corner aids with mass extraction from the vane cavity into the main flow as well as improves drag reduction.

4.5.1 Species and Efficiency. The modifications to the layout do not produce much of a change on the emissions of the model compared to the baseline model as seen in Table 11. In two loading conditions the model produces more CO than the baseline case for the same amount of CO_2 . However, in the other three loading conditions the trend is reversed. The slight increase in the CO on the lower loading conditions could stem from the inlets pushing out the combustion gases in the vane cavity. With the higher loading conditions the pressure gradient is probably better developed with the increased main loading, hence the slight reduction on the higher loading conditions. A real benefit of the nozzle configurations will be seen in the pattern and profile factor discussion on the higher loading conditions.

The most noticeable improvement with these modifications is that the pressure loss has decreased significantly in every loading condition. This decreased pressure loss could result from the introduction of a rounded exit to the vane cavity on the aft corner. The improvements range from 15% to a maximum 25% reduction on

the HMHP loading condition. The combustion efficiency has little change in this configuration. The unburned fuel at the exit plane is slightly increased which leads to the lower combustion efficiency which could also stem from the combustion gases being expelled from the vane cavity by these new inlets.

Table 11: Species and Efficiency Data for the Nozzle Model Compared to the Baseline Model Data

	$CO(ppm)$	$NO_x(ppm)$	$CO_2(\%)$	$O_2(\%)$	$UHC(ppm)$	$\eta_b(\%)$	$\frac{dP}{P}\%$
Baseline-1	1148	38.5	3.8	14.9	111	95.4	5.6
Nozzle-1	1280	38.1	3.8	14.9	110	95.3	4.7
Baseline-2	1335	55.6	3.7	15.0	74	96.2	3.6
Nozzle-2	1476	54.0	3.7	14.9	69	96.2	3.0
Baseline-3	284	10.7	1.8	18.1	33	97.2	7.9
Nozzle-3	270	11.3	1.8	18.2	39	96.8	6.3
Baseline-4	366	14.1	2.3	17.4	36	97.5	5.0
Nozzle-4	330	14.8	2.4	17.2	46	97.1	3.9
Baseline-5	2044	90.9	4.4	13.9	39	96.9	2.7
Nozzle-5	1779	80.6	4.4	13.9	36	97.2	2.3

4.5.2 Internal Flow Investigation. The geometry of this configuration is evident in Figure 24. The blue lines that are visible coming from the right are the inlets from the leading edge of the vane. These inlets introduce lower temperature flow into the vane cavity from the main air inlet. The concept was to draw the hot temperature combustion gases lower into the vane cavity by the pressure gradient created by the high speed flow resulting from the lowest vane inlets. In this model it is apparent that these inlets have dislodged some of the hot cavity gases that were found to be in the vane cavities of the other models. In Figure 10 on the baseline model, the hot gases that were found to be stable in the vane cavity. As seen in Figure 24 the stable gases have been pushed out slightly by the added inlets. However, the main cavity flow is not altered significantly with the modifications to the vane as is seen in Figure 25. However, it is seen that the additions of the air inlets have modified the flow from the main cavity to the vane cavity. There is a region of cool air that lies between the vortex coming over the top of the vane and the vane itself. This region

of lower temperature air could be used to reduce the temperatures inside the vane cavity where they are generally found to be above 2000 K in the other models.

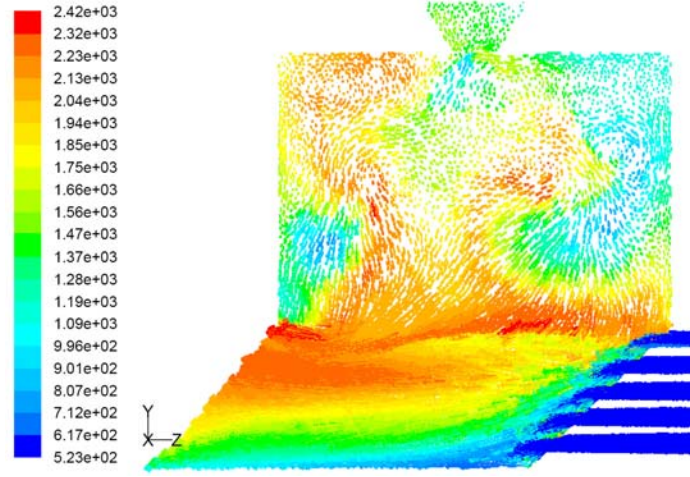


Figure 24: Velocity Vectors Colored by Temperature on Same Axial Plane with Front Air Inlet of Nozzle Model for LMLP Loading Condition

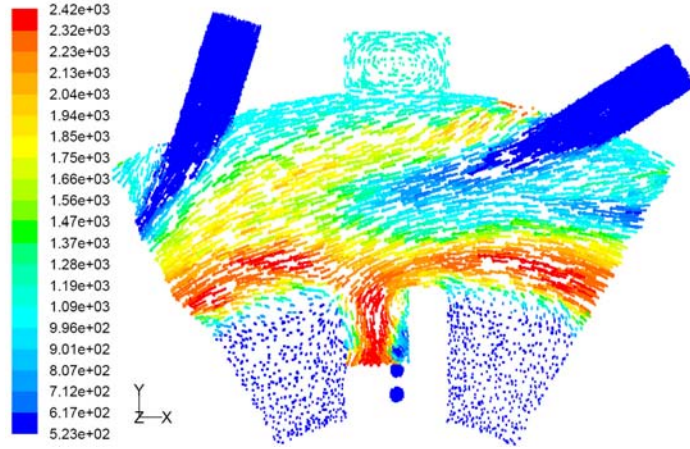


Figure 25: Velocity Vectors Colored by Temperature on Same Axial Plane with Front Air Inlet of Nozzle Model for LMLP Loading Condition

4.5.3 Pattern and Profile. The pattern factor is moderately increased with the nozzle configuration on the lower cavity loading parameters as seen in Table 12. For the higher cavity loading conditions it is observed that there is in fact a slight decrease in the pattern factor. This model was the only model tested that was able to decrease the loading factor. The reduction is the result of the pressure gradient

created in the vane cavity pulling the cavity combustion gases lower into the vane cavity. This in combination with the rounded aft corner was able to move the hot gases down while creating smoother flow from the vane cavity into the main flow.

Table 12: Pattern and Profile Data for Nozzle Model compared to the Baseline Model Data

	$T_{4avg}(K)$	$T_{mr}(K)$	Pattern Factor	Profile Factor
Baseline-1	1153	1741	0.91	0.34
Nozzle-1	1158	1848	1.05	0.52
Baseline-2	1155	1768	0.93	0.34
Nozzle-2	1157	1857	1.07	0.51
Baseline-3	869	1160	1.14	0.27
Nozzle-3	865	1142	1.08	0.29
Baseline-4	925	1218	0.99	0.24
Nozzle-4	940	1253	0.82	0.30
Baseline-5	1262	1879	0.83	0.36
Nozzle-5	1263	1953	0.87	0.49

The profile factor is more conclusive. The profile factor has increased in all the loading parameters. This increase is most visible in the lower cavity loading models where the profile factor has been increased by $\sim 50\%$. In Figure 26 the average circumferential temperatures are presented. The maximum average circumferential temperatures for the lower loading conditions are up to 100 K above the base model. The high cavity loadings produce similar maximum values to the baseline condition with the maximum temperatures lying within 5% of the baseline model.

The nozzle model works best at high loading conditions. The high speeds of the flow through the vane inlets indicate some performance improvements are achieved with the modifications. With the lowered CO levels and the reduced pressure loss at high loading conditions this configuration shows that there are some improvements that were obtained with the modifications to the vane.

4.6 Tall Vane Model

The final modification of the UCC has taken the base cavity layout and increased the height of the vane. The increase in vane height is important for scaling up the

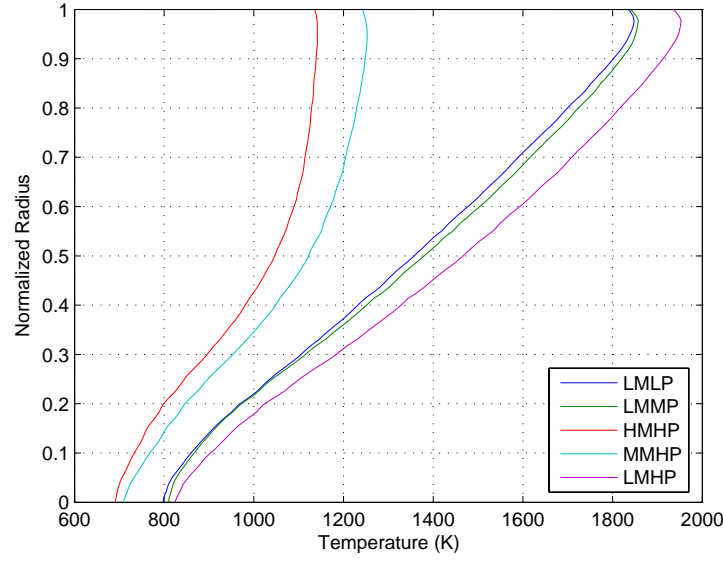


Figure 26: Average Circumferential Temperatures at the Exit Plane for the Nozzle Model on the Five Loading Conditions

UCC to the full size engine combustor and ITB usage. Many different layouts for the increased vane height model were attempted, including the variation of the cavity inlet location as well as a modification of the sweepback of the vane cavity rake-back; however, the optimal design was found to be the layout presented here. The height of the vane was increased by 11.7 mm to an overall height of 25.4 mm with the a cavity length of 38.1 mm, the same as the baseline model, as well as that model's cavity height. The sweepback of the vane cavity was maintained at 45° .

For comparisons to the other configurations the CLP, from Equation 15, was matched to the baseline configuration for each loading condition. To match the CLP the \dot{m}_{cav} was increased by 24% to compensate for the increased volume of the cavity. The fuel mass flow rate was also increased to match the equivalence ratio in the cavity of the baseline configuration. The mass flux of the cavity and the main inlets were held constant, which resulted in an increase in area for the cavity inlets. Matching of the mass fluxes will work in keeping the circumferential velocities consistent with the shorter vane models. The mass flow rate of the main inlet was 220% of the original vane models due to the increased inlet annulus area associated with the taller vane.

This led to a reduction in the ratio of cavity air flow to total air flow by $\sim 35\%$ compared to the baseline model.

4.6.1 Species and Efficiency. Surprisingly, the increased mass flow rates for the tall vane produced much lower efficiencies. The CO and UHC values at the exit plane were lower for four of the five loading conditions. However, the ppm values at the exit plane do not take into account the extra fuel that was injected into the cavity to match the equivalence ratios. To better match these values among the different configurations and understand why the efficiencies are so much lower in this model, the emissions indices will be used for the following comparisons. The emissions indices, EI, are the amount of pollutant produced per fuel injected and are used to better compare the different combustors' emissions data on differing operating conditions.

The tall vane produced significantly higher amount of EI_{CO} and $EI_{C_{12}H_{23}}$ compared to the baseline model as is seen in Table 13. This likely is the result of poorer mixing that happens in the larger cavity. The volume of the cavity has increased by 24% due to the larger inner radius of the taller vane and this increases the distance between the air inlets. The larger cavity on this model places the air inlets farther away from the fuel also. These increased distances decrease the fuel air mixing in the cavity which is seen to increase both the emissions indices for both carbon monoxide and the unburned fuel. These indices are in fact about 50% higher with this configuration than was seen with the baseline model.

The amount of CO_2 and O_2 is an indicator of the reaction that takes place within the combustor. These values are also somewhat skewed by the nature of the modifications to the model. The fuel and air injected into the cavity were increased by 24% to match the equivalence ratio and the CLP. However, the main air flow was increased by $\sim 220\%$. The extra O_2 mass flow from the main air flow is working to dilute the combustion products. That is why the O_2 levels are elevated, whereas the CO_2 levels are reduced by up to 50%.

Table 13: Species and Efficiency Data for the TallVane Model Compared to the Baseline Model Data

	EI_{CO}	$NO_x(ppm)$	$CO_2(\%)$	$O_2(\%)$	$EI_{C_{12}H_{23}}$	$\eta_b(\%)$	$\frac{dP}{P}\%$
Baseline-1	57.1	38.5	3.8	14.9	32.8	95.4	5.6
TallVane-1	78.8	25.4	2.3	17.3	47.3	93.4	3.1
Baseline-2	67.5	55.6	3.7	15.0	22.1	96.2	3.6
TallVane-2	90.8	34.4	2.2	17.4	34.9	94.4	2.0
Baseline-3	30.8	10.7	1.8	18.1	21.4	97.2	7.9
TallVane-3	47.8	9.9	1.1	20.1	32.1	96.0	5.0
Baseline-4	30.9	14.1	2.3	17.4	18.1	97.5	5.0
TallVane-4	61.4	13.1	1.7	19.5	32.1	95.4	3.0
Baseline-5	88.8	90.9	4.4	13.9	10.1	96.9	2.7
TallVane-5	134	54.9	2.6	16.7	15.7	95.3	1.5

The pressure loss term is also far lower for this tall vane model than for the baseline model. As was previously discussed the TallVane configuration is experiencing poorer mixing, leading to much higher levels of unburned fuel at the exit plane. The pressure loss term combines the hot and cold losses, but the reduction in the pressure loss term most likely comes from the hot loss reduction. With less fuel being reacted, the bulk acceleration of combustion gases decreases, which can lead to the significant reduction in pressure drop. Also, it can be assumed that the cold losses, or the drag of the gas in combustor, are not reduced by the large amount seen here with the modifications to the model.

4.6.2 Internal Flow Investigation. A slice of the cavity in Figure 27 shows that the tall vane behaves very much like the base and other models. The cavity contains a large portion of hot gases that are being sent down into the vane cavity. The hottest temperatures are evident at the interface between the cavity and the main air flow as well as the flow that comes over the vane and into the vane cavity. Also, the larger air inlets are seen by the increased amount of cooler air that is visible on the right and left side of the cavity in shot compared to the other models.

Figure 28 shows the lateral view of the flow. The temperatures again show that the vane cavity is not being fully utilized and has the largest amount of lower

temperature air of the models investigated. The hot combustion gases stay up in the vane cavity and little hot mass is sent down this cavity. The behavior of the flow inside the main cavity is similar to that of the other models in that the hot gases are occupying the volume between the air inlets. Also, the flow swirls over the vane and into the vane cavity as was observed in the other shorter models.

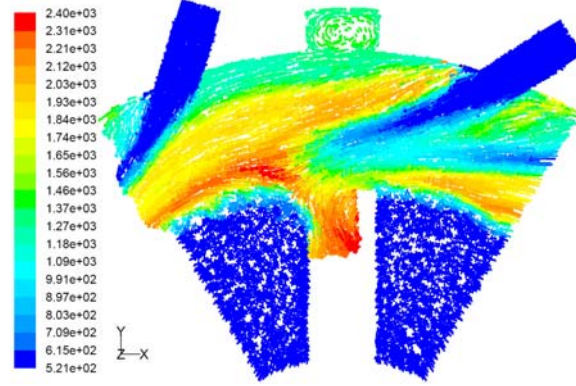


Figure 27: Tall Vane Plane in line with the Front Cavity Air Inlets

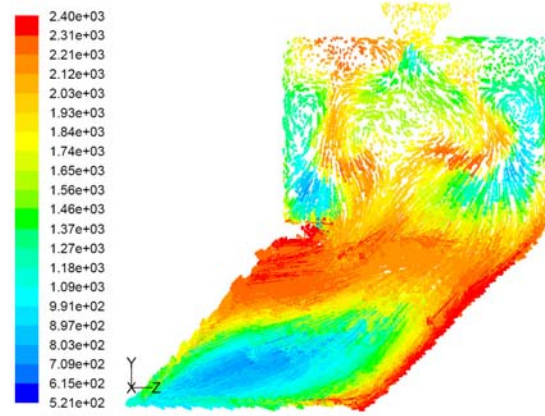


Figure 28: Velocity Vectors Colored by Temperature on Same Axial Plane with Front Air Inlet of TallVane Model for LMLP Loading Condition

4.6.3 Pattern and Profile. When Greenwood increased the exit area the pattern factor increased by a significant amount [8]. This is experienced with the tall vane model used here. The pattern factor increases $\sim 70\%$ on the tall vane model. The increase in pattern factor comes from the inability of the hot mass to be moved down radially. This coupled with the failure of the main flow to mix with the

combustion products, will work to keep the pattern factor much higher than on the other models. Figure 28 effectively shows this phenomenon from the side. In Figures 29 and 30 the high temperatures are seen to stay in the higher radial values. The higher radial temperatures resemble the outlet contours for the base model in Figure 13. The flow closer to the centerbody consists of much lower temperature gas and does not resemble much that has been investigated in this research.

Table 14: Pattern and Profile Data for TallVane Model compared to the Baseline Model Data

	T_{avg}	T_{mr}	Pattern Factor	Profile Factor
Baseline-1	1153	1741	0.91	0.34
TallVane-1	918	1655	1.64	0.68
Baseline-2	1155	1768	0.93	0.34
TallVane-2	920	1669	1.70	0.69
Baseline-3	869	1160	1.14	0.27
TallVane-3	741	1053	1.90	0.49
Baseline-4	925	1218	0.99	0.24
TallVane-4	824	1205	1.47	0.45
Baseline-5	1262	1879	0.83	0.36
TallVane-5	983	1740	1.45	0.61

The profile factor is also significantly higher than the base model. The profile factors are all about twice as high as the base model in all the loading conditions. Figure 29 indicates that the temperature profiles are disorganized with a lower temperature region in the mid-radial locations, not the uniform plot that Lefebvre indicates would be ideal [13]. The increased temperatures at the minimum radial locations result from the hot gases exiting the vane cavity down the front of the front rake-back. This can be seen in Figure 28. The maximum circumferential temperatures are lower than the baseline models but the lower average temperatures on the exit plane of the TallVane model work to increase the pattern and profile factors on all loading conditions.

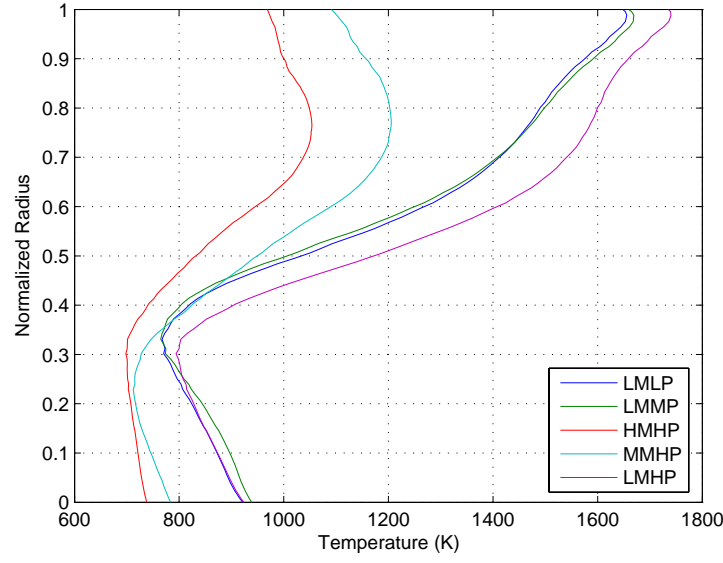


Figure 29: Average Circumferential Temperatures at the Exit Plane for the TallVane Model on the Five Loading Conditions

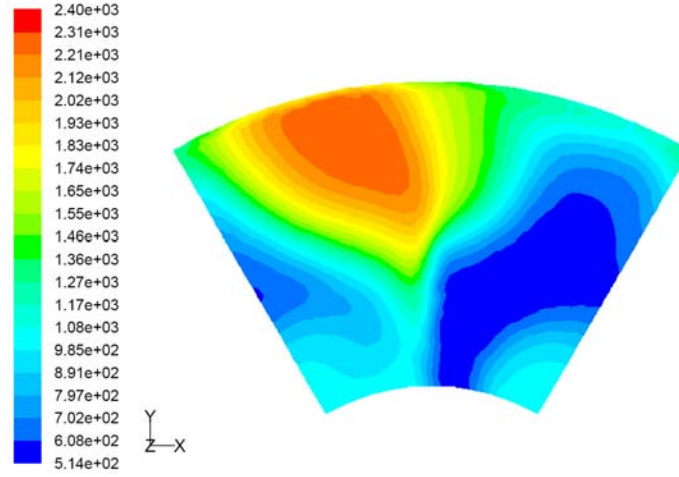


Figure 30: Temperature Contours on the TallVane Model with LMLP Loading Condition at the Exit Plane

4.7 Circumferential Velocity Calculations

The high g-loading of the cavity gases strongly influences the high flame propagation speeds of the UCC. The circumferential velocities that drive the high g-loading found in the cavity are a result of many factors. The length of the cavity, the angle of the cavity air inlets and the loading of the cavity all influence the circumferential

velocities. In Figure 31 the circumferential velocities are related to the CLP, from Equation 15, and a general trend can be seen. The average circumferential velocities increase with higher CLP.

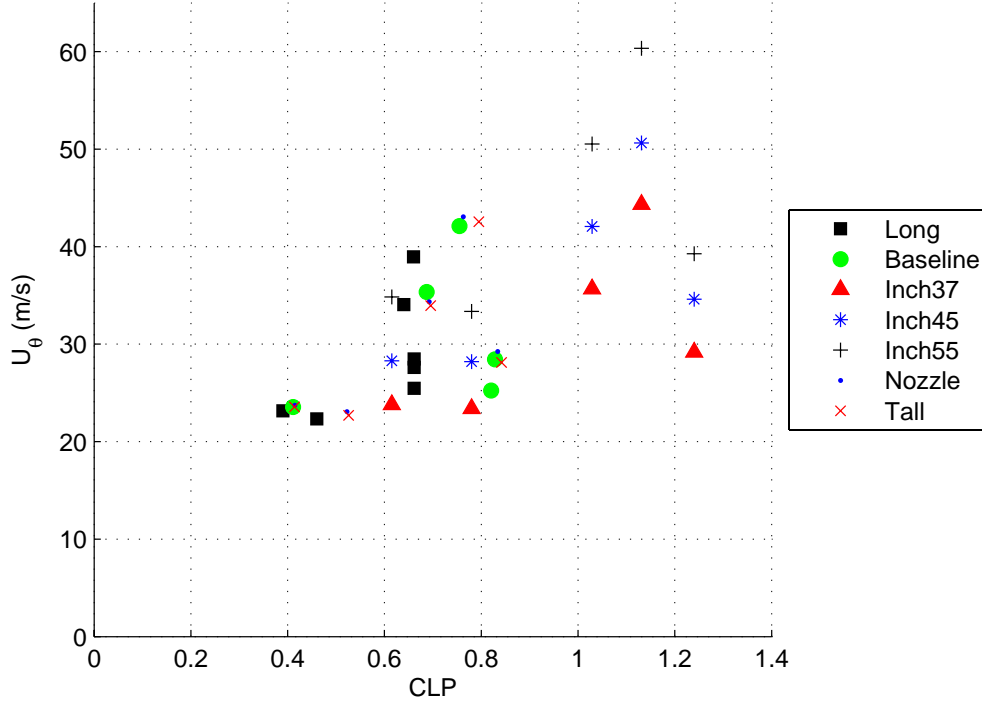


Figure 31: Circumferential Velocity vs CLP

On the shortest cavity with the 55° inlet scheme the average circumferential velocities are nearly 50% larger than the baseline model. The tall vane and the nozzle both share the same length cavity but do not experience significantly different circumferential velocities even though they are greatly different configurations. The length of the cavity seems to play a less important role in the circumferential velocity magnitude than the cavity loading. The air inlet angle has a greater influence on the circumferential velocities than the cavity length. On the HMHP loading condition on the 25.4 mm cavity with 37° air inlet angle the average circumferential velocity was found to be 44.4 m/s. On the higher air inlet models the circumferential velocities went to 50.6 m/s and 60.4 m/s on the 45° and 55° respectively. This 40%

increase in circumferential shows that the air inlet angle plays a significant role in the circumferential velocities of the UCC.

4.8 Emissions Comparisons

The emissions data was compared to the g-loading as defined in 20 where R is the average radial value for the cavity. The U_θ used for the g-load was calculated using the average circumferential velocities in the cavity. These values are plotted against CLP in Figure 31. The shorter cavity with the 55° model had a average velocity that was significantly higher than the others and the g-loading was calculated to be $\sim 8000 - g$.

In Figure 32 the mass weighted mole fraction of NO_x is plotted against the g-loading. The trend shows that with increasing g-loading the amount of NO_x in the exhaust decreases quickly.

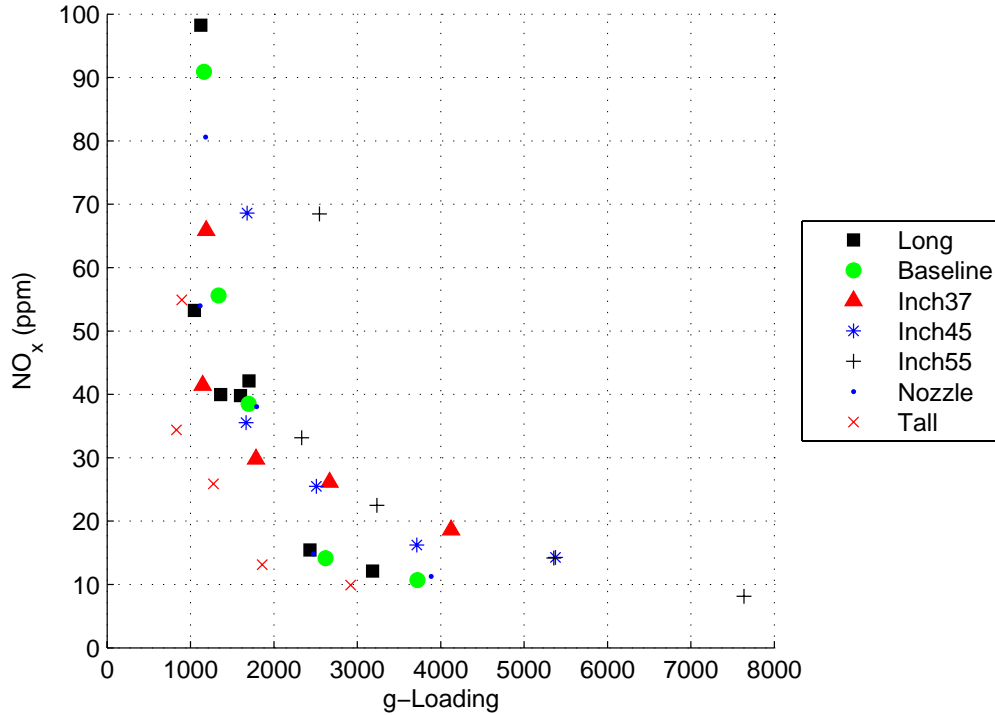


Figure 32: NO_x on the Exit Plane vs g-loading

Similar CO trends are seen in Figure 33. The graph shows that the CO amounts decrease as the g-loading increases. This is an indication that the numerical model is burning the fuel more completely as the fuel droplet residence time in the cavity is increased. This corresponds to CO abatement principles by keeping the residence times longer in the cavity to reach a more complete reaction.

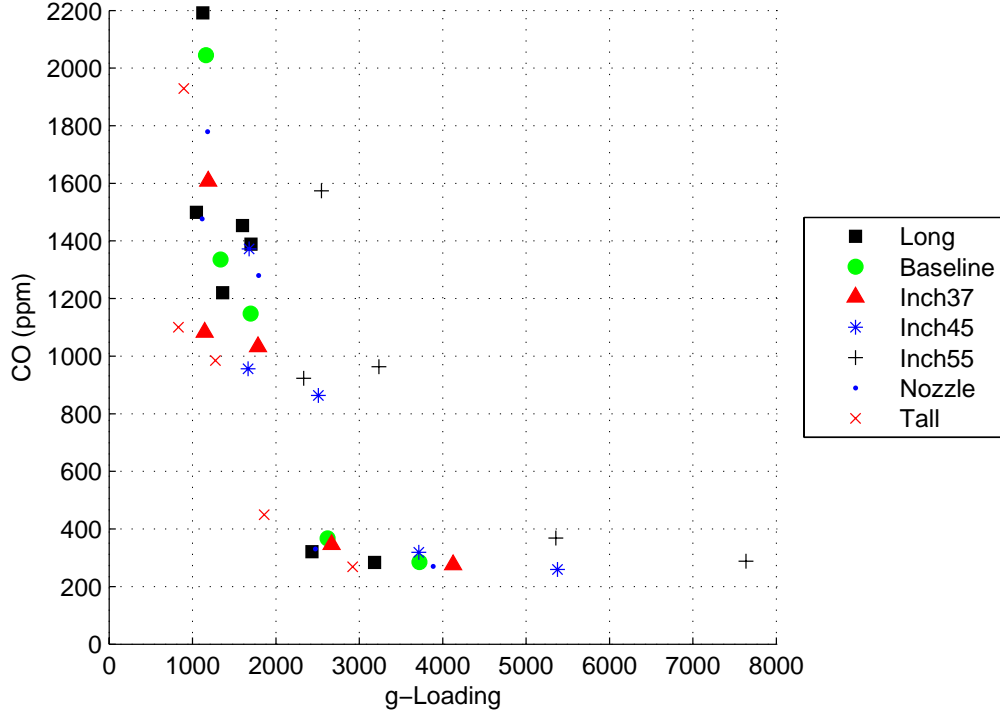


Figure 33: Carbon Monoxide on the Exit Plane vs g-loading

4.9 Profile Comparisons

The LMLP loading conditions were compared on the seven different geometries to investigate how the different models temperature profiles match. In Figure 34 it is shown that there is a wide variety of temperature profiles on the seven models.

The three red trendlines correspond to the shortest cavity models with varying air inlet angles. The highest air injection angle, 55° , provides a smoother, more steady temperature increase than the other two 25.4 mm cavity models. The 45°

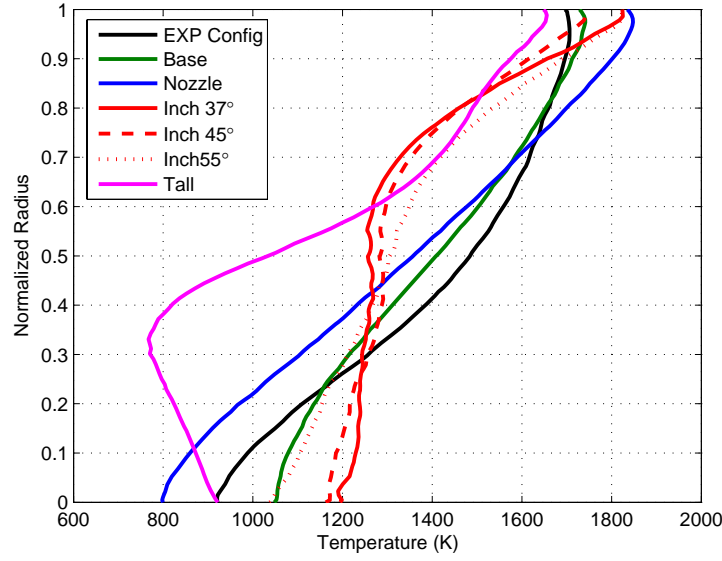


Figure 34: Average Circumferential Temperatures at the Exit Plane for the Seven Models on the LMLP Loading Condition

angle model shows the best of these temperature profiles with the lowest maximum temperature. In addition to the lower T_{mr} the highest minimum temperature is found on this model; this corresponds to a minimum temperature spread.

The baseline cavity length models show a large difference in behavior. The baseline model shows an improvement over the experimental geometry model with T_{mr} dropping by 5%. The nozzle model provides a lower minimum temperature and a higher maximum temperature than the base model leading to poorer profile factors.

The tall vane model shows that the T_{mr} has been reduced. However, between 0 and 0.35 on the non-dimensionalized radius the mean circumferential temperatures are actually dropping below that of the inner temperatures. The temperatures then increase to the T_{mr} at higher radial values.

V. Conclusions

5.1 *Research Overview*

Numerical simulations on modification to the Ultra Compact Combustor (UCC) have been conducted. A commercial computational fluid dynamics (CFD) package was used to compare the flow characteristics against experimental data as well as other loading and boundary condition features. Experimentally, the UCC has been tested at AFRL/PRTC using several different configurations. The use of CFD analysis aids in determining design parameters faster and with lower expenses than experimental tests can provide.

The numerical model was first validated by comparing the experimental data to the output of a numerical model. Then the use of periodic boundaries and grid density were tested to see the impact that these modifications had on the simulation. Following this validation process the numerical UCC configuration was modified several times. A shorter cavity from previous numerical work became the new baseline. From this new standard cavity configuration an improved aerodynamic vane and a taller vane were investigated. In addition to these investigations, the cavity was shortened and the air inlet angle was increased twice from the baseline 37° to 45° and 55° .

5.2 *Results Synopsis*

Shortening the cavity length to 25.4 mm reduced the amount of CO produced for all loading conditions. This came at the cost of higher UHC at the exit plane and higher pressure loss. Pattern and profile factor also suffered with significant increases found in all cases. The smaller cavity did show a more complete usage of the cavity volume with hot gases and the smaller size making the modifications of this model more appealing.

When the angle of the air inlets was increased to 45° further benefits were seen with CO production as well as a drop in NO_x quantities on all five loading conditions.

This reduction over all loading conditions was not seen in the shortened cavity with 37° inlet model. Surprisingly, the UHC increase with the higher inlet angle of 45° on some loading conditions. This model also produces lower profile factors that were decreased by $\sim 30\%$ from the 37° inlet model. When the air inlet's angle was increased further to 55° many of the benefits from 37° to 45° were lost. The pressure loss, at 55° , continued to increase to the highest levels found in this research. The CO levels increased to levels seen on the original 37° air inlet model. The largest benefit of this 55° model is that the amount of UHC found in the exhaust reduced 33% compared to the 37° model.

On the baseline model holes were included in the leading edge of the vane that connects to the vane cavity. The vane cavity was also altered to improve the aerodynamics of hot flow as it exited the vane cavity. This model predicts very large drops in pressure loss compared to the baseline model. The inlets appear to be disrupting the hot gases in the vane cavity which led to an increase in the pattern factor and an increase in the harmful emissions on some loading conditions.

Increasing the height of the vane is an important step in enabling the UCC to be used as a ITB. The vane's height was increased 11.7 mm to a total of 25.4 mm. Mass flux terms were kept the same along with CLP to maintain comparability to the other models in this research. The pattern factor increased by 70% compared to the baseline configuration. This was the result of the inability to drive the hot mass down to lower radial values. The CO in the exhaust is comparable to the baseline model but the pollutant emissions indices are $\sim 50\%$ higher than the baseline model.

The numerically modeled UCC indicated that with increased g-loading the CO and NO_x both show signs of a general reduction. This compliments the data that shows the circumferential velocity increases with an increased cavity loading parameter.

On the whole, considering emissions, size of combustor and temperature distribution, the model configurations that shows the best behavior was the shortened,

25.4 mm cavity with the 45° air inlets. The performance improvements are seen on for the CO , the NO_x and an increase in U_θ . The combination of the reduced harmful emissions and the smaller combustor make this configuration the best model of the models considered.

5.3 *Future Work*

Work continues on the UCC to optimize the configurations and methods of testing.

Time accurate solutions should be run on the numerical model because of limitations with the equilibrium solver and the perceived inaccuracies from the steady solution.

The aerodynamically improved vane had significantly lower pressure loss compared to the other models. Rounding of the aft portion in the vane cavity could result in reduction of pressure losses in other UCC models. Possible combination of the rounded edge and the shorter cavity could reduce pressure loss; this combination would be ideal since the high pressure losses are one of the shorter cavity's main drawbacks.

Vane curvature is still a significant item of interest. For the implementation of the aero Inter Turbine Burner (ITB) vane curvature will be needed to combine the stators with the combustor. An analysis of the curvature and the resultant flow will be essential in putting a working model together for the ITB.

The angle and location of the air inlets appear to have a large impact on the flow behavior. Further study to investigate these parameters should be conducted to see if there is an improvement with further angles and locations of the air injection.

Also, the models should be run on a larger spectrum of loading conditions. There should be more effort in investigating lower and higher equivalence ratios to determine the effects of lean and rich operating conditions on the UCC.

Finally, the tall vane needs to be modified to improve the mixing and spreading of the hot exit gases. The hot combustion gases are located in a small portion of the exit plane and spreading this out will improve the pattern factor which will lead to improved turbine lifetime.

Appendix A. Additional Numerical Data

A.1 Extra Tables

Table A.1: Species and Efficiency Data for the Coarse Model Compared to the Experimental Data

	$CO(ppm)$	$NO_x(ppm)$	$CO_2(\%)$	$O_2(\%)$	$\eta_b(\%)$	$\frac{dP}{P}\%$
Expr-1	1089	37.3	3.2	16.4	97.5	5.0
Coarse-1	1454	39.8	3.8	14.8	95.6	5.9
Expr-2	1264	48.2	3.7	15.7	97.7	3.3
Coarse-2	1499	53.2	3.8	14.9	96.4	3.8
Expr-3	478	15.6	1.6	18.7	98.0	8.3
Coarse-3	285	12.1	1.8	18.2	97.3	8.6
Expr-4	524	27.3	2.3	17.7	97.9	5.1
Coarse-4	321	15.4	2.2	17.5	97.8	5.1
Expr-5	1962	58.9	4.3	14.9	96.4	3.0
Coarse-5	2192	98.2	4.5	13.9	97.0	2.9

Table A.2: Case 1 (LMLP) Loading Condition for the Different Model Configurations

	Coarse	Baseline	Inch37	Inch45	Inch55	Nozzle	TallVane
$CO(ppm)$	1454	1148	1032	863	964	1297	984
$NO_x(ppm)$	39.8	38.5	29.8	25.5	22.5	38.1	25.4
$CO_2(\%)$	3.8	3.8	3.7	3.7	3.7	3.8	2.3
$O_2(\%)$	14.8	14.9	15.0	15.1	15.0	14.9	17.3
$UHC(ppm)$	92.4	111	182	204	150	110	97.9
Pattern Factor	1.0	0.91	1.1	1.0	0.97	1.0	1.6
Profile Factor	0.29	0.34	0.54	0.45	0.52	0.52	0.68
$\eta_b(\%)$	95.6	95.4	93.4	93.0	94.5	95.3	93.4
$U_\theta(\frac{m}{s})$	28.4	28.4	29.2	34.6	39.3	29.2	28.1
$\frac{dP}{P}(\%)$	5.9	5.6	5.9	5.8	6.0	4.7	3.1

Table A.3: Case 2 (LMMP) Loading Condition for the Different Model Configurations

	Coarse	Baseline	Inch37	Inch45	Inch55	Nozzle	TallVane
$CO(ppm)$	1500	1336	1082	956	923	1476	1100
$NO_x(ppm)$	53.2	55.6	41.4	35.5	33.1	54.0	34.4
$CO_2(\%)$	3.8	3.7	3.7	3.6	3.7	3.7	2.3
$O_2(\%)$	14.9	15.0	15.0	15.1	15.0	14.9	17.4
$UHC(ppm)$	62.1	73.4	119	147	103	69.4	70.9
Pattern Factor	0.99	0.93	1.1	1.1	1.0	1.1	1.7
Profile Factor	0.28	0.34	0.58	0.43	0.53	0.51	0.69
$\eta_b(\%)$	96.4	96.2	95.1	94.5	95.8	96.2	94.4
$U_\theta(\frac{m}{s})$	22.3	25.2	23.4	28.2	33.4	23.1	22.7
$\frac{dP}{P}(\%)$	3.8	3.6	3.8	3.8	3.8	3.0	2.0

Table A.4: Case 3 (HMHP) Loading Condition for the Different Model Configurations

	Coarse	Baseline	Inch37	Inch45	Inch55	Nozzle	TallVane
$CO(ppm)$	285	285	276	259	288	270	268
$NO_x(ppm)$	12.1	10.7	18.6	14.3	8.2	11.3	10.0
$CO_2(\%)$	1.8	1.8	1.8	1.7	1.8	1.8	1.0
$O_2(\%)$	18.2	18.1	18.2	18.2	18.1	18.2	20.1
$UHC(ppm)$	31.2	33.2	46.3	31.8	6.23	38.8	26.9
Pattern Factor	0.99	1.1	1.3	1.4	1.5	1.1	1.9
Profile Factor	0.18	0.27	0.71	0.44	0.54	0.29	0.49
$\eta_b(\%)$	97.3	97.2	96.3	97.3	98.9	96.8	96.0
$U_\theta(\frac{m}{s})$	39.0	42.1	44.4	50.6	60.4	43.1	42.5
$\frac{dP}{P}(\%)$	8.6	7.9	8.0	8.3	8.6	6.3	5.0

Table A.5: Case 4 (MMHP) Loading Condition for the Different Model Configurations

	Coarse	Baseline	Inch37	Inch45	Inch55	Nozzle	TallVane
$CO(ppm)$	321	367	346	320	368	330	449
$NO_x(ppm)$	15.4	14.1	26.1	16.2	14.2	14.8	13.1
$CO_2(\%)$	2.2	2.3	2.3	2.3	2.3	2.4	1.7
$O_2(\%)$	17.5	17.4	17.4	17.4	17.3	17.2	19.5
$UHC(ppm)$	30.7	36.1	56.3	47.8	10.4	45.9	39.4
Pattern Factor	0.88	0.99	1.1	1.2	1.3	0.82	1.5
Profile Factor	0.21	0.24	0.66	0.43	0.54	0.30	0.45
$\eta_b(\%)$	97.8	97.5	96.5	97.0	98.8	97.1	95.4
$U_\theta(\frac{m}{s})$	34.1	35.4	35.7	42.1	50.5	34.4	34.0
$\frac{dP}{P}(\%)$	5.1	5.0	5.2	5.5	5.6	3.9	3.0

Table A.6: Case 5 (LMHP) Loading Condition for the Different Model Configurations

	Coarse	Baseline	Inch37	Inch45	Inch55	Nozzle	TallVane
$CO(ppm)$	2193	2045	1608	1372	1573	1779	1929
$NO_x(ppm)$	98.2	90.9	65.9	68.6	68.5	80.6	54.9
$CO_2(\%)$	4.5	4.4	4.4	4.4	4.4	4.4	2.6
$O_2(\%)$	13.5	13.9	13.9	13.9	13.9	13.9	16.7
$UHC(ppm)$	28.1	39.0	76.3	79.2	47.9	36.0	37.6
Pattern Factor	0.80	0.83	0.86	0.82	0.76	0.87	1.5
Profile Factor	0.37	0.36	0.57	0.39	0.46	0.49	0.61
$\eta_b(\%)$	97.1	96.9	96.4	96.6	97.2	97.3	95.3
$U_\theta(\frac{m}{s})$	23.2	23.5	23.8	28.3	34.8	23.7	23.6
$\frac{dP}{P}(\%)$	2.9	2.7	2.9	2.9	3.0	2.3	1.4

Table A.7: DPM Wall Interaction Comparison on Baseline Model with LMLP Loading Conditions

	Wall Jet	Trapped	Reflect
$CO(ppm)$	1147	1492	1162
$CO_2(\%)$	3.8	3.8	3.8
$O_2(\%)$	14.9	14.8	14.9
$NO_x(ppm)$	38.5	39.1	40.5
$UHC(ppm)$	110	74	109
$\eta_b(\%)$	95.4	96.1	95.4
Pattern Factor	0.91	0.96	0.90
Profile Factor	0.34	0.32	0.32
$\frac{dP}{P}(\%)$	5.6	5.6	5.6
$U_\theta(m/s)$	28.4	28.4	29.4

Appendix B. Emissions and Profile

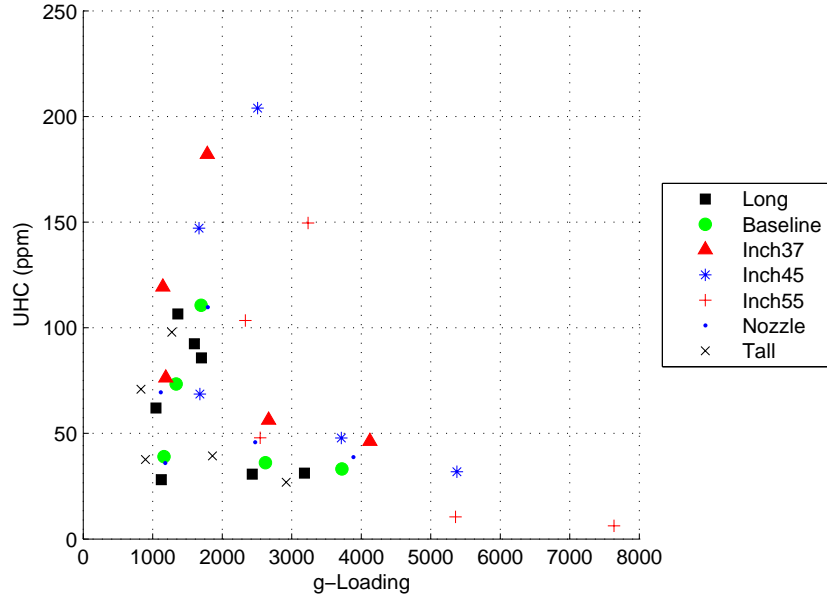


Figure B.1: Unburned Hydrocarbons on the Exit Plane vs g-loading

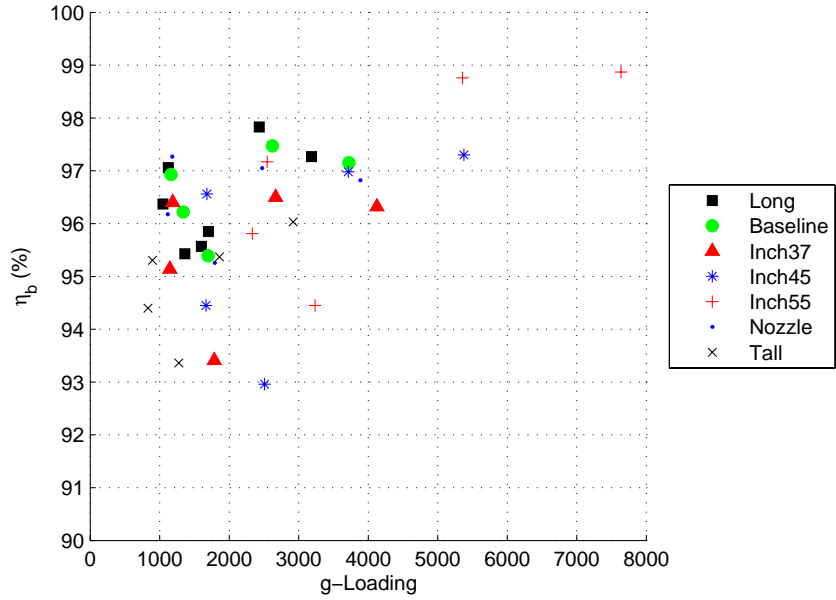


Figure B.2: Combustion Efficiency on the Exit Plane vs g-loading

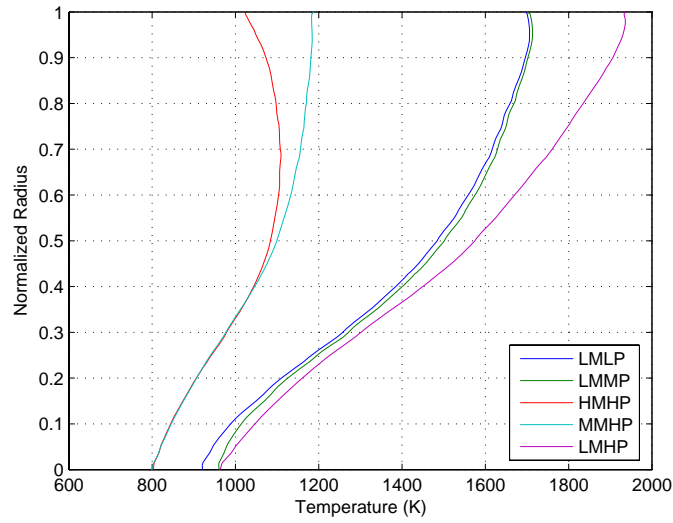


Figure B.3: Average Circumferential Temperatures at the Exit Plane for the Coarse Model on the Five Loading Conditions.

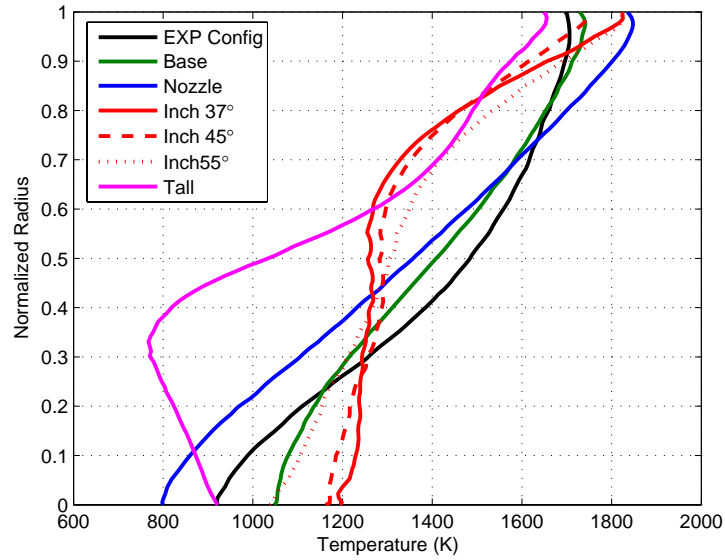


Figure B.4: Average Circumferential Temperatures at the Exit Plane for the Seven Models on the LMLP Loading Condition

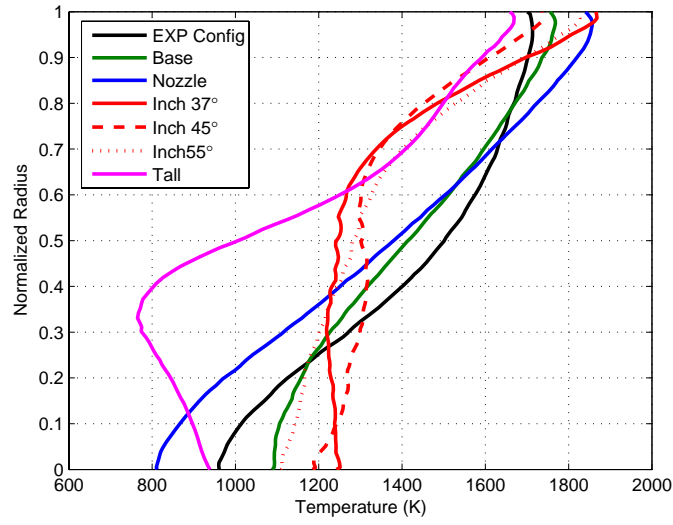


Figure B.5: Average Circumferential Temperatures at the Exit Plane for the Seven Models on the LMMP Loading Condition

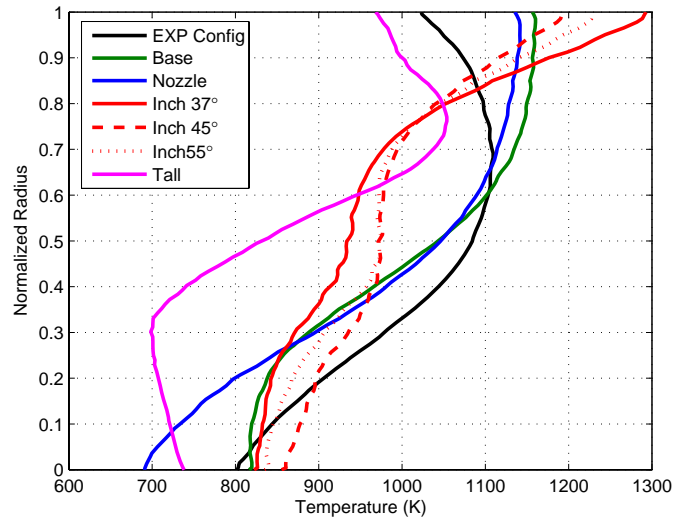


Figure B.6: Average Circumferential Temperatures at the Exit Plane for the Seven Models on the HMHP Loading Condition

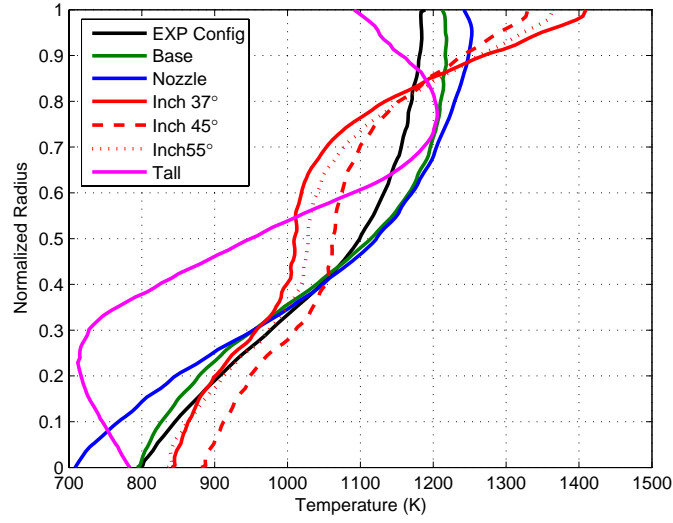


Figure B.7: Average Circumferential Temperatures at the Exit Plane for the Seven Models on the MMHP Loading Condition

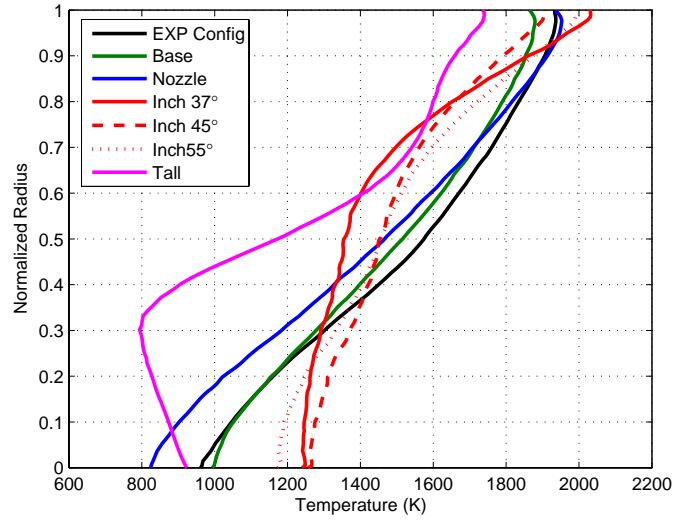


Figure B.8: Average Circumferential Temperatures at the Exit Plane for the Seven Models on the LMHP Loading Condition

Bibliography

1. Anderson, J. Tannehill. D. and R. Pletcher. *Computational Fluid Mechanics and Heat Transfer*. Hemisphere Publishing Corporation, Washington, second edition, 1997.
2. Anthenien, R.A., R.A. Mantz, W.M. Rouquemore, and G. Sturgess. "Experimental Results for a Novel, High Swirl, Ultra Compact Combustor for Gas Turbine Engines". Air Force Research Laboratory, Wright-Patterson AFB, OH.
3. Armstrong, Jason M. *Effect of Equivalence Ratio on G-Loading on In-situ Measurements of Chemiluminescence in an Ultra Compact Combustor*. Master's thesis, Graduate School of Engineering, Air Force Institute of Technology (AETC), Wright-Patterson AFB OH, March 2004. AFIT/GAE/ENY/04-M01.
4. ARP1533. "Procedure for the Calculation of Gaseous Emissions from Aircraft Turbine Engines". *Society of Automotive Engineers*, June 1996.
5. Bernard, Peter S. and James W. Wallace. *Turbulent Flow*. John Wiley and Sons, Hoboken, NJ, first edition, 2002.
6. Blazek, J. *Computational Fluid Dynamics: Principles and Applications*. Elsevier Science, Kidlington, Oxford, UK, second edition, 2004.
7. Fluent Inc, Lebanon, NH. *Fluent Users Guide*, 6.2 edition, 2005.
8. Greenwood, Roger. *Numerical Analysis and Optimization of the Ultra Compact Combustor*. Master's thesis, Graduate School of Engineering, Air Force Institute of Technology (AETC), Wright-Patterson AFB OH, March 2005. AFIT/GAE/ENY/05-M10.
9. Heywood, John B. *Internal Combustion Engine Fundamentals*. McGraw-Hill, 1988.
10. Hill, Phillip G. and Carl R. Peterson. *Mechanics and Thermodynamics of Propulsion*. Addison-Wesley Publishing Company, second edition, 1992.
11. Incropera, Frank P. and David P. DeWitt. *Fundamentals of Heat and Mass Transfer*. John Wiley and Sons, third edition, 1990.
12. Kuo, Kenneth K. *Principles of Combustion*. John Wiley and Sons, second edition, 2005.
13. Lefebvre, Arthur H. *Gas Turbine Combustion*. Hemisphere Publishing Corporation, West Lafayette, IN, 1983.
14. Lewis, George D. *Centrifugal-Force Effects on Combustion*. Pratt and Whitney Aircraft, West Palm Beach, Florida.

15. Lewis, George D. *Swirling Flow Combustion Fundamentals and Application*. Technical report, AIAA Paper No.73-1250.
16. Little, B.H. and R.R. Whipkey. "Locked Vortex Afterbodies". *Journal of Aircraft*, Volume 16, No. 5, May 1979.
17. Liu, Feng and William Sirignano. "Turbojet and Turbofan Engine Performance Increase Through Turbine Burners". 2000-0741. AIAA, May 2000.
18. Mawid, M. A., T. W. Park, H. Thornburg, B. Sekar, and J. Zelina. "Numerical Analysis of Inter-Turbine Burner(ITB) Concepts for Improved Gas Turbine Engine Performance". volume AIAA 2005-1162.
19. Oates, Gordon C. *Aerodynamics of Aircraft Engine Components*. American Institute of Aeronautics and Astronautics, 3rd edition, 1992.
20. Pointwise Inc. *Gridgen V15*, 2004.
21. Quaale, Ryan J. *Experimental Results for a High Swirl, Ultra Compact Combustor for Gase Turbine Engines*. Master's thesis, Graduate School of Engineering, Air Force Institute of Technology (AETC), Wright-Patterson AFB OH, March 2003. AFIT/GAE/ENY/03-5.
22. Rouquemore, W.M., D. Shouse, D. Burrus, A. Johnson, C. Cooper, B. Duncan, K.-Y. Hsu, V.R. Katta, G.J. Sturgess, and I. Vihinen. "Trapped Vortex Combustor Concept for Gas Turbine Engines". *AIAA 2001-0483*, Jan 2001.
23. Sirignano, W. A. and F. Liu. "Performance Increases for Gas-Turbine Engines Through Combustion Inside the Turbine". *Journal of Propulsion and Power*, Volume 14, No. 6, May 1998.
24. Straub, D.L., T.G. Sidwell, D.J. Maloney, K.H. Casleton, and G.A. Richards. "Simulations of a Rich Quench Lean (RQL) Trapped Vortex Combustor". Presented at the AFRC International Symposium, Sept 2000.
25. Yonezawa, Y., H. Toh, S. Goto, and M. Obata. "Development of the Jet-Swirl High Loading Combustor". *AIAA-90-2451*.
26. Zelina, Joseph, G.J. Sturgess, Adel Mansour, and Robert D. Hancock. "Fuel Injector Design for an Ultra-Compact Combustor". *ISABE-2003*.

Vita

Jonathan Anisko was born in Philadelphia, Pennsylvania. He graduated from the Worcester Academy in Worcester, Massachusetts. From there he attended The Pennsylvania State University in University Park, Pennsylvania where he graduated with a Bachelor of Science in Aerospace Engineering. Lt Anisko received his commission through ROTC at Detachment 720.

Jonathan Anisko was first assigned to the National Air and Space Intelligence Center (NASIC), Wright Patterson AFB, as a developmental engineer. He was almost immediately selected for NASICs Watson Scholar Initiative and re-assigned to the Air Force Institute of Technology. Upon graduation, he will be assigned back to NASIC for a three-year tour.

REPORT DOCUMENTATION PAGE				Form Approved OMB No. 074-0188	
<p>The public reporting burden for this collection of information is estimated to average 1 hour per response, including the time for reviewing instructions, searching existing data sources, gathering and maintaining the data needed, and completing and reviewing the collection of information. Send comments regarding this burden estimate or any other aspect of the collection of information, including suggestions for reducing this burden to Department of Defense, Washington Headquarters Services, Directorate for Information Operations and Reports (0704-0188), 1215 Jefferson Davis Highway, Suite 1204, Arlington, VA 22202-4302. Respondents should be aware that notwithstanding any other provision of law, no person shall be subject to a penalty for failing to comply with a collection of information if it does not display a currently valid OMB control number.</p> <p>PLEASE DO NOT RETURN YOUR FORM TO THE ABOVE ADDRESS.</p>					
1. REPORT DATE (DD-MM-YYYY) 23-03-2006		2. REPORT TYPE Master's Thesis		3. DATES COVERED (From – To) SEP 04 – MAR 06	
4. TITLE AND SUBTITLE Numerical Investigation of Cavity-Vane Interactions within the Ultra Compact Combustor				5a. CONTRACT NUMBER	
				5b. GRANT NUMBER	
				5c. PROGRAM ELEMENT NUMBER	
6. AUTHOR(S) Anisko, Jonathan, F., 2d Lt, USAF				5d. PROJECT NUMBER	
				5e. TASK NUMBER	
				5f. WORK UNIT NUMBER	
7. PERFORMING ORGANIZATION NAMES(S) AND ADDRESS(S) Air Force Institute of Technology Graduate School of Engineering and Management (AFIT/EN) 2950 Hobson Way WPAFB OH 45433-7765				8. PERFORMING ORGANIZATION REPORT NUMBER AFIT/GAE/ENY/06-M01	
9. SPONSORING/MONITORING AGENCY NAME(S) AND ADDRESS(ES) AFOSR/NA Dr. Julian Tishkoff 801 N. Randolph Street Arlington VA 22203-7765				10. SPONSOR/MONITOR'S ACRONYM(S)	
				11. SPONSOR/MONITOR'S REPORT NUMBER(S)	
12. DISTRIBUTION/AVAILABILITY STATEMENT APPROVED FOR PUBLIC RELEASE; DISTRIBUTION UNLIMITED.					
13. SUPPLEMENTARY NOTES					
14. ABSTRACT A numerical analysis and design optimization of the Ultra Compact Combustor (UCC) has been conducted. The UCC is a combustor designed to incorporate high-g loadings to increase flame propagation speed while reducing flame length, thereby helping to significantly reduce the size of a combustor. Since real experimental tests are expensive and construction time is prohibitive to test many different design configurations, CFD modeling of the UCC is used to speed up the design optimization process while reducing the overall costs. The CFD models have been validated by comparison to data from recent experimental tests. The use of periodic sections and grid independence were validated as well. Modifications to the physical configuration were then modeled using CFD. The shortening of the cavity was found to reduce the harmful emissions in the exhaust. Increasing the angle to 45° and 55° of the air inlets further improved the emissions by increasing the residence time of the fuel particles in the cavity. Aerodynamically improving the vane reduced the pressure loss of the combustor by up to 25%. The increased vane height was an initial step in scaling up the UCC to operational configurations. Of the models in this research, the most improved configuration was found to be the 45° air inlet on the shortest cavity.					
15. SUBJECT TERMS Combustion, Combustors, Computational Fluid Dynamics, Emission, Efficiency					
16. SECURITY CLASSIFICATION OF:			17. LIMITATION OF ABSTRACT	18. NUMBER OF PAGES	19a. NAME OF RESPONSIBLE PERSON
REPORT	ABSTRACT	c. THIS PAGE			Ralph A. Anthenien, PhD, USAF (ENY)
U	U	U	UU	99	19b. TELEPHONE NUMBER (Include area code) (937) 255-3636, ext 4643